Tailoring mechanical properties of AlSi9Cu3(Fe) alloy via heat treatments in PBF-LB Processing

Materials & Design 258 (2025) 114591

Contents lists available at ScienceDirect

Materials & Design

journal homepage: www.elsevier.com/locate/matdes

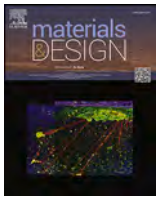

Tailoring mechanical properties of AlSi9Cu3(Fe) alloy via heat treatments in PBF-LB Processing☆

Lagalante Ilaria [a,*], Martucci Alessandra [a], Manfredi Diego Giovanni [a,b], Fino Paolo [a,b], Lombardi Mariangela [a,b]

[a] Department of Applied Science and Technology (DISAT), Politecnico Di Torino, Corso Duca degli Abruzzi 24, Torino 10129, Italy
[b] Center of Integrated Additive Manufacturing (IAM), Politecnico di Torino, Corso Castelfidardo, 51, 10138 Torino, Italy

1. Introduction

Aluminium and its alloys are highly valued for their low density, strong mechanical properties, great corrosion resistance, and high thermal conductivity, making them ideal for a large number of applications, from automotive to aerospace [1]. Their performance and properties are designed based on alloying elements, resulting in Al-based alloys that exhibit a wide range of characteristics [2,3]. One of the most common alloying elements is silicon, a key element in casting alloys thanks to improved fluidity and reduced shrinkage, though it forms diamond crystal structure particles that degrade mechanical properties [4,5]. Other common elements are copper, whose addition to Al-Si-Mg alloys further boosts strength and hardness thanks to precipitation hardening [6,7], and iron, which is used to improve temperature resistance, though excessive amounts can reduce ductility and promote brittle phases [8]. Indeed, a critical iron content for Al alloys has been defined depending on the silicon content, i.e. 0.075 x [%Si] – 0.05; iron amount that exceeds the critical content can lead to defects and alloy embrittlement [9].

Al alloys are already extensively used in traditional processes such as wrought and casting. However, new technologies such as Powder Bed Fusion Laser Beam (PBF-LB) have surfaced in the past decades, broadening the possibilities of both part design and material performance. This process overcomes design limitations, enabling the production of complex geometries such as cooling channels and lattice structures. In addition, the fast cooling rate, i.e. 10^5-10^6 K/sec, creates an incredibly fine granulometry and a supersaturated solution, enhancing the alloy performance. For instance, Si solubility is usually negligible at room temperature; however, the fast cooling rates during the process increase it significantly, up to 8 %, which makes the solution very saturated, but also unstable and particularly sensitive to heat treatments [10]. Many studies have focused on the LPBFed aluminium response to heat treatments. Traditional heat treatments for cast alloys such as T6 (solubilisation + quenching + artificial ageing) have been widely discussed for LPBFed Al alloys, especially for alloys with Cu and Mg, which are reinforced by precipitation strengthening. However, the different microstructure in LPBFed alloys required a customisation of temperatures and holding time of the treatments, since the high temperatures homogenise the microstructure but lose the initial strengthening due to the peculiar fine microstructure. Later on, adapted heat treatments such as direct ageing (T5) and other bespoke treatments were developed to improve the material characteristics without overlooking the microstructure, but instead trying to accommodate it [1,11].

One alloy that has been widely studied for cast production is the alloy AlSi9Cu3(Fe) (ENAC-46000). This alloy is a high-performance alloy that has already been diffused in many automotive applications such as pistons and heat exchangers. Material performance requirements have been dictated by BS EN 1706:2020 + A1:2021 standard, i.e. tensile strength (UTS) of 240 MPa, yield strength (YS) of 140 MPa, minimum elongation at fracture (e) of 1 % and hardness of 80 HBW, which is about 92 HV according to ASTM E140-12B(2019)e1. The presence of Cu makes it suitable for heat treatments to strengthen the material. However, AlSi9Cu3(Fe) alloy generally exhibits low plasticity because of the brittle Si particles and Fe-rich compounds [12,13]. Although it has been extensively studied for casting production, AlSi9Cu3(Fe) has only recently been employed for PBF-LB production [14–16] and few heat treatments have also been tested, as resumed in Table 1.

Roudnicka et al. [12] studied the precipitation strengthening mechanism upon T5, focusing on a treatment at 140 °C for 26 h, and upon a conventional T6, reporting an improvement of strength after both heat treatments, mainly associated with precipitation strengthening, though having a worse elongation at fracture after T5. Fiocchi et al. [16,18] tested a similar alloy, which had a smaller amount of Fe,

☆ This article is part of a special issue entitled: 'Additive Manufacturing' published in Materials & Design.

* Corresponding author.
E-mail address: ilaria.lagalante@polito.it (L. Ilaria).

https://doi.org/10.1016/j.matdes.2025.114591
Received 5 March 2025; Received in revised form 24 July 2025; Accepted 13 August 2025
Available online 15 August 2025

Table 1
State-of-art on AlSi9Cu3(Fe) produced by PBF-LB, with details of heat treatments and tensile tests results.

Ref.	Process Parameters	Alloy Condition	YS (MPa)	UTS (MPa)	ε (%)
[15]	P = 400 W v = 1330	As-built	219.0 ± 20.0	374.0 ± 11.0	1.9 ± 0.2
[17]	mm/s hd = 0.15	Stress Relieving (300 °C/ 2 hrs)	~220.0	~340.0	~2.2
[12]	mm lt = 0.05 mm	T5 (140 °C/26 hrs)	300.0 ± 18.0	395.0 ± 14.0	1.7 ± 0.1
		T6 (520 °C/6 hrs + water quench + 160 °C/10 hrs)	326.0 ± 23.0	380.0 ± 13.0	2.6 ± 0.2
[14]	P = 350 W v = 1200	As-built (powder A1)	228.0 ± 2.0	455.3 ± 1.3	5.1 ± 0.1
	mm/s hd = 0.12 mm lt = 0.05 mm	As-built (powder B1)	253.7 ± 2.7	486.7 ± 4.7	5.3 ± 0.3
[16]	P = 275 W v = 2250	As-built	266.1 ± 0.1	462.5 ± 3.0	4.5 ± 0.1
	mm/s hd = 0.09 mm	T6 (470 °C/6 hrs + water quench + 160 °C/24 hrs)	206.0	318.7	7.8
[18]	lt = 0.03 mm	250 °C/ 8 hrs	231.8 ± 1.5	380.5 ± 1.2	4.8 ± 0.5
		250 °C/ 64 hrs	229.5 ± 1.1	380.3 ± 0.7	5.8 ± 0.1

treated at 250 °C for different times, focusing on the characterisation of the ones treated for 8 and 64 h, and also treated with a conventional T6. The latter was found to significantly enhance the material ductility, although it reduced its strength. On the other hand, the treatment at 250 °C was optimized with a holding time of 8 h, having a lower strength and a slightly better elongation. However, although these heat treatments have acceptable results, they show some limitations: the T5 and the annealing are particularly long, making them less suitable for industrial applications. In addition, the T6 treatment, commonly used to enhance the strength of traditionally produced Al-Si-Cu alloys, has been reported to cause an intensive porosity increase, possibly due to incipient fusion of Al_2Cu or hydrogen diffusion during the high-temperature stage, usually over 450 °C [12,19,20].

The present study systemically explores the influence of different heat treatments on the microstructure of a PBFed AlSi9Cu3(Fe), and therefore on its mechanical behaviour, an area that remains insufficiently explored in the current literature. Indeed, while previous studies have primarily focused on the as-built condition or on traditional, impractically long heat treatments, the present research targets industrially feasible, short-duration heat treatments within a temperature range that has not been sufficiently investigated, comprehensively analysing their impact on the microstructural evolution via image analysis, X-ray diffraction (XRD), direct scanning calorimetry (DSC), EBSD, and the mechanical performance in comparison to the as-built condition. This integrated approach enables a deeper understanding on the control of precipitation behaviour through heat treatments and with the consequences on mechanical properties, providing practical insights for industrial applications and filling a clear gap left by prior works in the field. Furthermore, the research allows to understand how to tailor the mechanical properties of the heat-treated PBFed AlSi9Cu3 (Fe) according to specific application needs, whether targeting increased strength or enhanced ductility, always maintaining the process industrially feasible.

At first, the parameter optimisation is carried out and the as-built microstructure is characterised in order to define the starting condition and to enable the systematic evaluation of the subsequent heat treatments by comparison. Various heat treatment temperatures were chosen according to the thermal response of the as-built alloy, with short holding time to meet the treatment feasibility. In particular, a T5 treatment at 190 °C for 1 to 8 h was considered to evaluate the alloy strengthening when treated for a shorter time, and different annealing treatments at higher temperatures, i.e. 250, 300 and 400 °C, were performed to try to improve the alloy ductility. Some of these treatments were further picked, and the tensile behaviour of heat treated samples was tested and discussed according to the microstructure evidence.

2. Materials and methods

The fully dense PBFed samples were fabricated using a commercial gas-atomised AlSi9Cu3(Fe) powder supplied by ECKA Granules Germany GmbH™. Powder particle size distribution (PSD) and morphology were measured using Morphologi 4 Malver Panalytical and Laser Diffraction Particle Size Analyzer (Mastersizer 3000, Malvern Panalytical). Regarding the latter, the volumetric PSD was evaluated via analysis of the diffraction angle of a laser when a small amount of powder flows through the chamber, whereas the former measures both PSD (numerically distributed) and powder morphology through optical image elaboration. The oxygen level in the powder was also verified using an elemental analysis instrument (ONH836, Oxygen/Nitrogen/Hydrogen Elemental Analyzer by LECO), while powder density was measured through a pycnometer (Ultrapyc 5000).

The powder was processed in an EOSINT M270 Dual-mode system (EOS GmbH) under an argon atmosphere, with oxygen levels below 0.1 %. To identify the optimum densification, 10x10x10 mm^3 cubic samples were produced and analysed following a multi-level DOE (Design Of Experiment) approach. Two levels of laser power (170 and 195 W), three levels of hatch distance (0.10, 0.12 and 0.14 mm) and four levels of scan speed (800, 1000, 1200, and 1400 mm/s) were tested, for a total of 24 sets of parameters. All samples were produced employing a scan strategy with a 67° rotation after each layer, and with an Al-based building platform heated to 100 °C. After the PBF-LB process, electro-discharge machining was used to remove the as-built specimens from the platform. The porosity was measured using the Archimedes principle for all samples. The analysis tool CAT was employed to identify relations between parameters and porosity and to pick the optimised set of parameters [21].

The following heat treatments were carried out: in detail, T5 treatments at 190 °C for different holding times, i.e. 1, 2, 4, and 8 h, and different annealing treatments at 250, 300 and 400 °C, each held for 0.5, 1, 2 and 4 h. All heat treatments were performed in air. The reasons behind the heat treatments design are discussed in paragraph 3.3.

Material characterisation was carried out using optical microscope (Leica DMI 5000 M™) and SEM (SEM EVO™ 15) for microstructure analysis along the building direction, with samples prepared using paper, silica, and finally etched using a Keller reagent for SEM imaging. Microhardness testing was performed on the XZ plane using a VMH Vickers tester with a 0.5 kgf load and a dwell time of 10 s, following ASTM E384, with five indentations per sample for repeatability. Thermal analysis was carried out through DSC using a 214 Polyma apparatus. DSC scans were performed in the 25–550 °C temperature range with a heating rate of 10 °C/min under a nitrogen-protective atmosphere.

Phase identification was conducted using XRD with a PANalytical™ X'Pert PRO PW3040/60 diffractometer on the as-built and annealed samples. XRD scans were performed with Cu-Kα1 radiation in the 2θ range of 10-150°, with a step size of 0.013° and a step duration of 60 s, and phase identification was performed using the X'Pert HighScore software. The XRD pattern was also used to measure the Al lattice parameter according to the cosθcotθ method.

On samples treated with selected heat treatments and on the as-built one, grain size distribution was assessed via EBSD maps recorded using a Tescan S9000G™ FIB-SEM, with a voltage of 20 kV and 10nA, a working distance of about 7 mm and a field of view of 70.8 μm, and a 70° sample tilt. The as-built and heat treated x-z planes were analysed. It should be noted that preliminary analyses of the as-built microstructure were reported in [22], which analysed the effect of traditional heat treatments

on machining and corrosion behaviour of the alloy. However, discussion on these analyses is further extended in the present work to improve the understanding of the effect of heat treatments on the microstructure.

Tensile tests were also performed on the as-built and heat treated samples with the same selected treatments. The specimens were designed according to ASTM E8, and built with the longitudinal axis parallel to the platform. Tests were performed at room temperature, with a preload of 3 MPa and a test speed of 0.008 1/s.

3. Results and discussion

3.1. Powder analysis

The powder used for the sample production was a commercial powder provided by Ecka Granules Germany GmbH. Its chemical composition, as provided by the producer, is reported in Table 2 in comparison to the one reported by the normative EN 1706:2020 + A1:2021 for AlSi9Cu3(Fe), alloy designation ENAC-46000. The oxygen level in the powder, verified through LECO analysis, is equal to 0.1040 ± 0.0005 %, confirming what was declared by the producer, i.e. 0.11 %. The density of the material was assessed at 2.76 g/cm^3 through pycnometer analysis.

The PSD of the powder was measured through two different technologies, i.e. static automated imaging and laser diffraction particle size analyser. The PSD resulting from both analyses are reported in Fig. 1. The imaging analysis (Fig. 1.a) revealed a finer fraction since it is a numeric evaluation, and by so, it highlights finer fractions, which might instead get lost in the volumetric one (Fig. 1.b) [23].

Image analysis through Morphologi 4 also allowed the evaluation of the morphology of the powder, represented through circularity in Fig. 2.a, where the circularity is defined as the ratio between the equivalent area circle and the area of a circle with the actual perimeter of the particle, meaning that the closer to 1, the more spherical the particle is. As can be seen, even though high, the measured values were not excellent. SEM images were analysed to investigate the powder morphology further (Fig. 2.b,c). As previously stated [22], irregularly shaped particles and a high number of satellites were spotted, which negatively affected overall sphericity. These powder irregularities might also affect the efficiency of the process: irregular shapes generally decrease powder flowability and packing efficiency [24,25], and satellites might lead to undesirable phenomena during the process, such as spattering, uneven recoating and also leading to a rougher final surface [26].

3.2. As-Built microstructure

Samples were then produced through PBF-LB technology. A multi-level factorial design was employed to evaluate the best parameters that ensured the highest densification level. In particular, two levels of laser power, three levels of hatch distance and four levels of scan speed were incorporated while maintaining all the other parameters constant for all specimens, as depicted in the Material and Methods section. At first, it was noted that the lower laser power, i.e. 170 W, implied a decreased final density of the samples for all sets of parameters, making the higher power, i.e. 195 W, more suitable to obtain denser samples (Table A1). The samples produced at 195 W showed an adequate low porosity, with a minimum of 0.17 % and a maximum of 2.2 %. The response of porosity as a function of hatch distance and scan speed, with a constant power of 195 W, is depicted in Fig. 3. Besides the laser power, the DOE analysis highlighted a significant correlation between porosity and scan speed, either on its own or in relation to hatch distance. It can indeed be observed how the final density tended to decrease when increasing the scan speed, especially at higher hatch distance, due to a lower energy density that might lead to lack of fusion [27]. However, an increase in porosity could also be observed at low scan speeds and low hatch distances. Indeed, the too-high energy density in this case could lead to overheating and the appearance of keyholes [28]. Accordingly, the optimised set of parameters was picked to be laser power of 195 W, scan speed of 800 mm/s and hatch distance of 0.14 mm.

The microstructure obtained with the optimised process parameter combination was observed through an optical microscope and in further detail through SEM confirming previous analyses [22]. As can be observed in Fig. 4.a,b, the characteristic fish-scale-shaped melt pools (MP) were clearly observable on the as-built surface along the building direction. Though showing an overall good density, some porosities could still be spotted, even though mainly of small scale and regular shape (Fig. 4.b). However, a few more significant and more irregular pores could be found, i.e. lack of fusion, which might have been caused by spattering phenomena or by unforeseen episodes during the process (Fig. 3.e,f). It was observed that the microstructure changed in the proximity of these lack of fusion, with coarser cellular structure in the MPs above the lack of fusions. This difference may result from the varying thermal conductivity of the air trapped in the keyhole pores compared to that of the fused solid material since the latter is higher, leading to better conduction of the heat generated during the melting [29,30]. Observing the MP with optical microscope at higher magnification allowed to identify the different cellular structures in the MP (Fig. 4.c,d), which becomes even more evident by SEM images (Fig. 5).

Indeed, the MP centre was characterised by a very dense and fine cellular structure, with an α-Al matrix surrounded by a eutectic Si network (Fig. 5.c,e). The same network can be seen at the MP boundaries, though bigger cells and thicker Si networks were observable, which were caused by the re-heating of the overlapped area during consequent layer melting (Fig. 5.d,f). The measured cell size (λ) was around 0.47 ± 0.15 μm in the MP centre and 1.04 ± 0.65 μm at its border. A cooling rate ($\dot{T}$) of one magnitude slower at the border (9.98E4 K/s) compared to the centre (1.10E6 K/s) was measured through the Matyja equation (*i.e.* $\lambda = 43.2\dot{T}^{-0.324}$), which correlates cooling rate and cell size [31,32]. It is also possible to identify a third area, just below the MP border, where the network was partially broken, with dispersed Si particles. This area, known as the Heat Affected Zone (HAZ), is considered an MP fine zone of the underlying layer that was altered by heat during the lasering of the top additional layer (Fig. 5.b) [29,33]. The different states of the Si network have been proven to influence the mechanical behaviour of the alloy. Tang et al. [34] reported a lower measured hardness at the MP boundary compared to its centre for an AlSi10Mg alloy, which was also seen to influence the ductile failure of the sample since the coarser cells make the area softer and lead to tearing.

XRD analysis was performed to observe the phases in the as-built material further (Fig. 6.a) [22]. The main peaks were identified as matrix α-Al and eutectic Si, which compose the cellular network. However, other minor phases could be identified, mainly the Al_2Cu compound, in good agreement with Fiocchi et al. [16]. These peaks had a very low intensity, and most pattern peaks were hidden below more intense ones, making their unequivocal definition more complex. The low intensity can be caused by their low presence and size in the as-built material

Table 2
Powder chemical composition as provided by the producer, compared to the one reported by the standard.

%wt	Si	Cu	Fe	Mg	Mn	Zn	Other	Al
Ecka DataSheet	9.3	3.0	0.91	0.29	0.21	0.81	–	Bal.
EN 1706:2020 + A1:2021 (E) (ENAC-46000)	8.0–11.0	2.0–4.0	<1.3	0.05–0.55	<0.55	<1.2		Bal

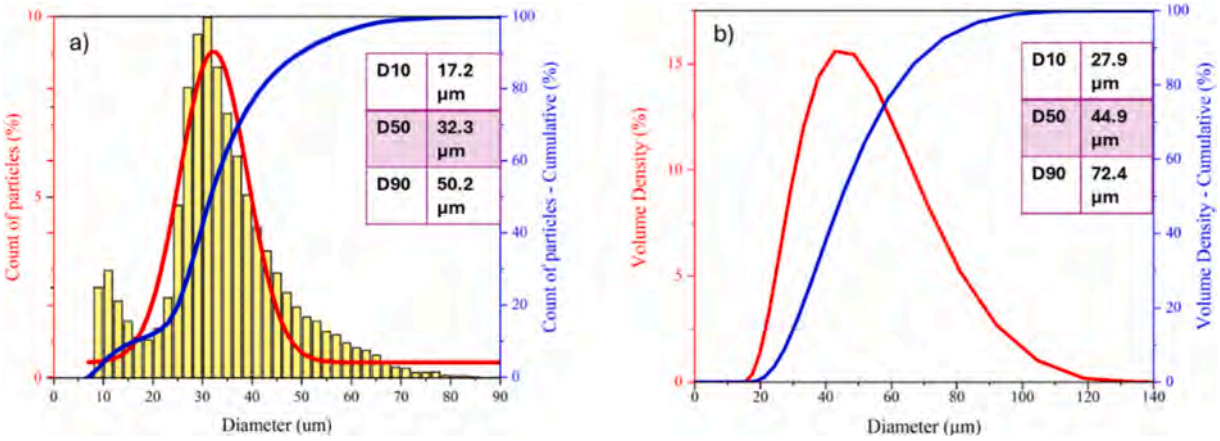

Fig. 1. PSD measured through image analysis with numeric distribution (a) and laser diffraction with volumetric distribution (b).

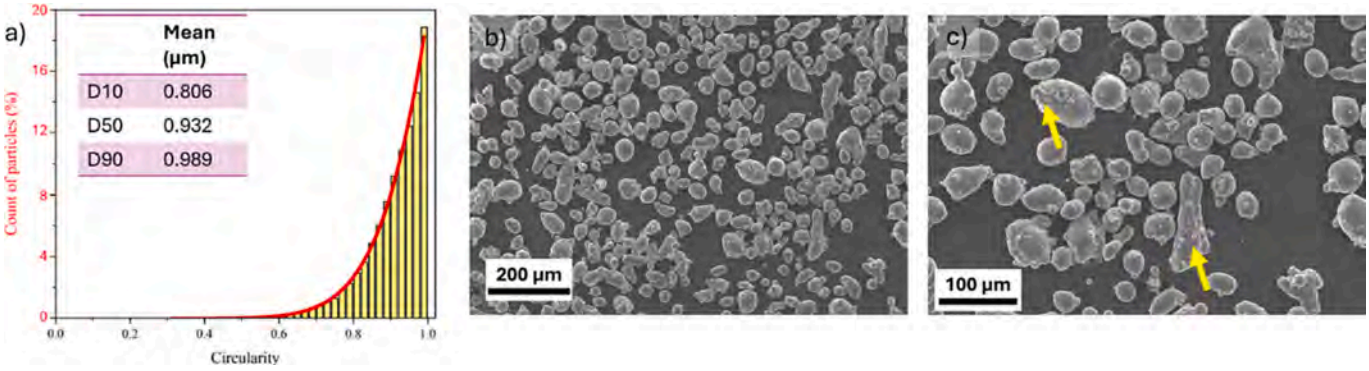

Fig. 2. a) Circularity of the powder, plotted as numeric distribution; b-c) SEM images of the powder.

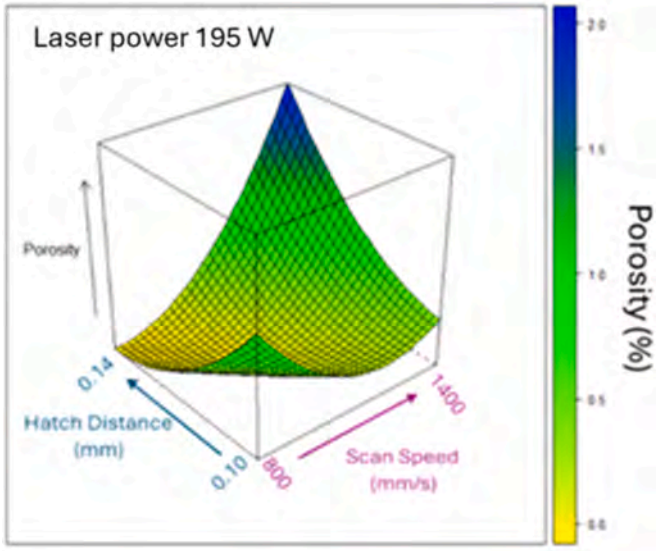

Fig. 3. Porosity response surface in relation to hatch distance and scan speed, having a constant 195 W laser power, as analysed by the DOE tool CAT.

since their precipitation was limited by the high cooling rate during the PBF-LB process. However, an observation can be made to validate the presence of Al_2Cu. There are two peaks at approximately 28.5° (peak A) and 47° (peak B), which were associated with the Si pattern at 100 % intensity, Si (111), and 55 % intensity, Si (220), respectively. Nonetheless, the two peaks have very similar intensities, i.e. 2.50 and 2.02 %, with peak B being 81 % of peak A. Notably, peak B can also be associated with the Al_2Cu (310) peak of 100 % intensity. At ~ 47°, Si and Al_2Cu peaks are very close to each other and display low signal. When the signal has low intensity, peaks become lower and larger; thus, the two different peaks cannot be recognised, but a single larger peak can be found. So, it can be presumed that Al_2Cu contributed to increasing the intensity of peak B, making it more similar to peak A. It was also possible to identify other small phases, with intensities lower than 1 %, presumably associable with other precipitates of the Al_2Cu precipitation sequence, i.e. AlCu, θ‘‘, θ’, θ and Al_3Cu_2, or other minor Al-Cu-Fe phases.

In addition, in order to correctly identify the proper temperatures for heat treatments, a DSC analysis was carried out, to observe the relevant temperatures of precipitation phenomena taking place while heating the as-built sample (Fig. 6.b) [22]. Four different exothermic peaks could be identified. The first, more prominent peak (A) was associated with the precipitation of both Si and θ’’, with an onset temperature of 189 °C and a peak temperature of 248 °C. Peaks B and D completed the precipitation sequence of the Al_2Cu phase, with peak B associated with the precipitation of θ’ (onset temperature of 312 °C) and peak D with the precipitation of θ (onset temperature of 456 °C). Peak C represented instead the spheroidization of previously precipitated Si phases. These peak assignments are in accordance with what was already observed by Fiocchi et al. for this composition [16]. In addition, according to [35], peak D can be otherwise associated with Al-Fe phase precipitation in an Al-Fe-Si alloy.

Grain size within the MPs was estimated through EBSD maps (Fig. 7). An average Feret diameter of 7.29 µm was measured, though it was possible to clearly distinguish two different types of grains in two distinct areas of the MP. Indeed, the MP borders were characterised by smaller and equiaxed grains, exhibiting a Feret diameter in the range of

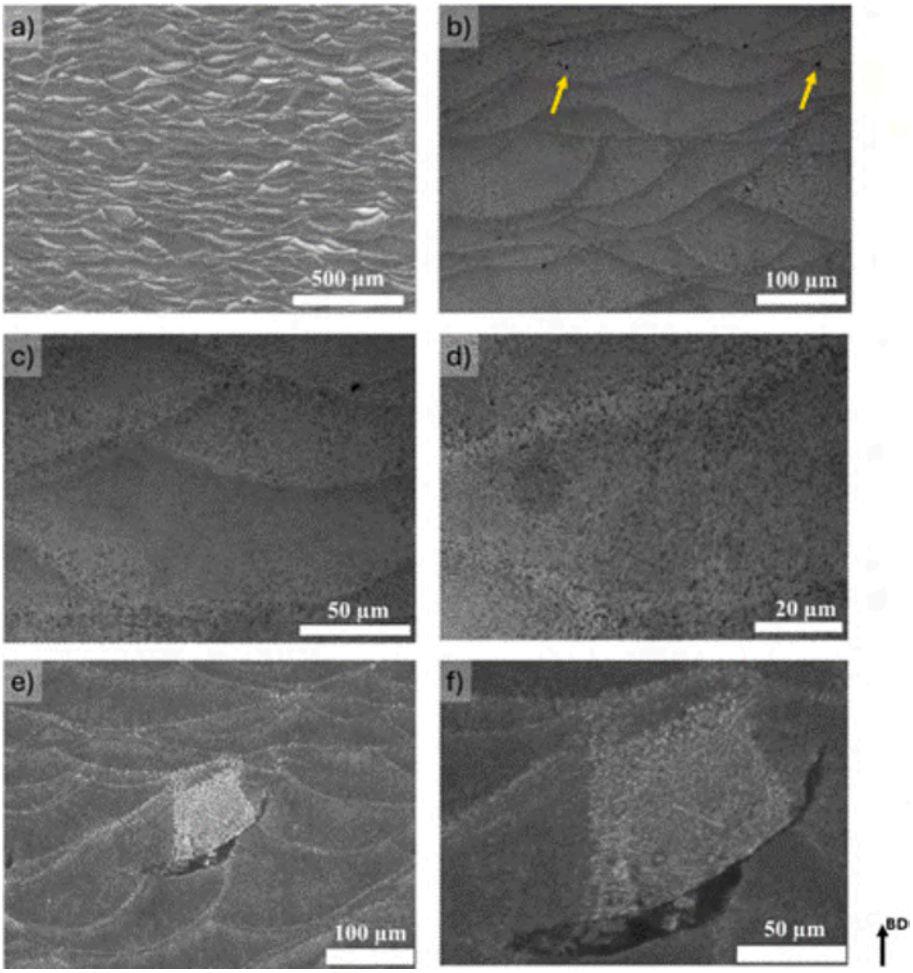

Fig. 4. Microstructure of the as-built alloy at different magnifications, with focus on a lack of fusion (e-f). Yellow arrows in (b) indicate pores. (For interpretation of the references to colour in this figure legend, the reader is referred to the web version of this article.)

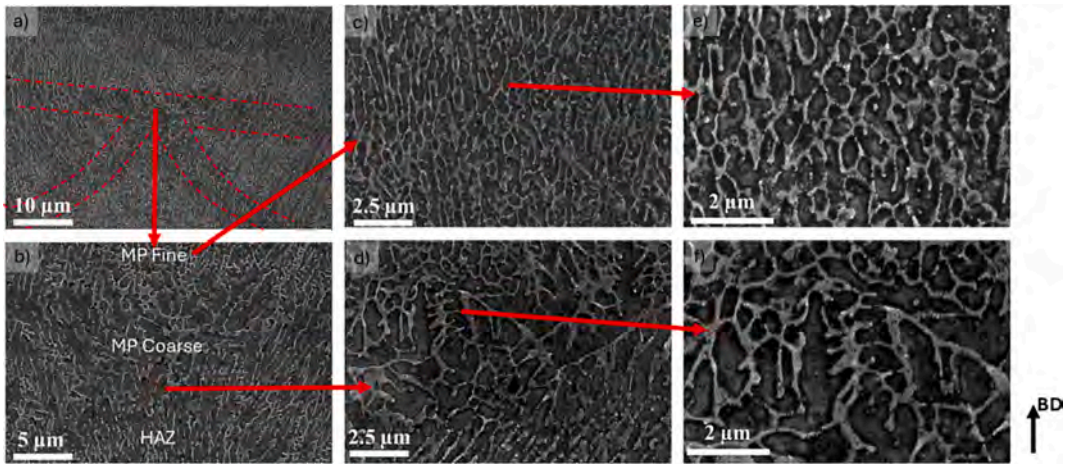

Fig. 5. SEM images of the as-built microstructure at different magnifications: (a-b) shows the different microstructural areas in the MP; (c-e) show the fine microstructure inside the MP; (d-f) show the coarser microstructure at the MP border.

0.5–5.0 µm. This resulted from the fastest heat conduction in the liquid–solid interface during the melting. On the other hand, elongated grains were observed at the MP centre, having a Feret diameter ranging from 50 µm to as much as 100 µm. Indeed, the slowest heat dissipation in this area lets the grains grow following the thermal gradient [15]. Finally, it must be noted that a preferential {001} texture could be observed, though not very strong and with a small MUD parameter, below 4. This was caused by the applied scanning strategy during the sample production, i.e. 67°: indeed, this strategy tended to interrupt the columnar grain growth, resulting in a weaker texture [36].

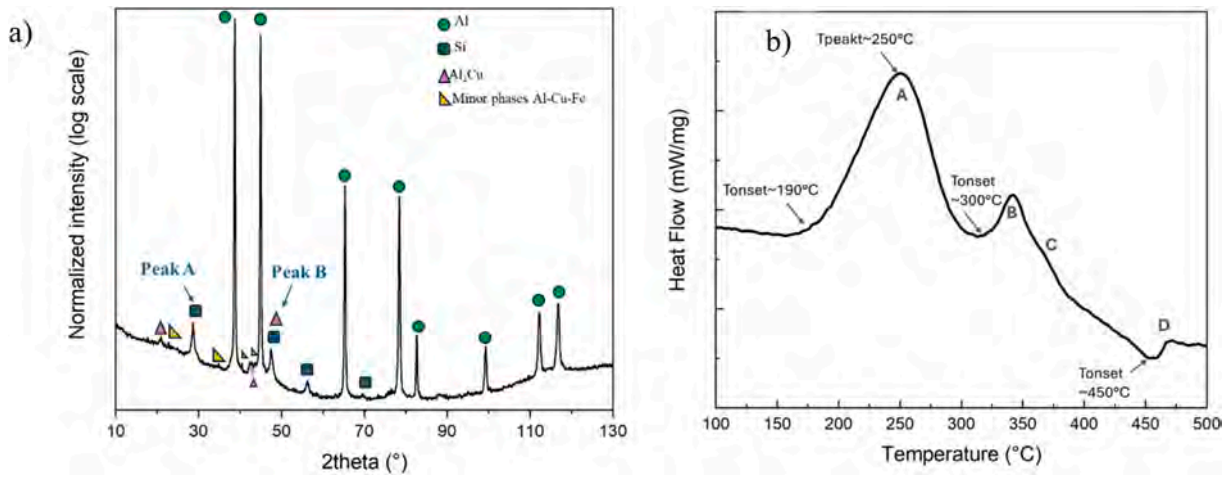

Fig. 6. (a) XRD pattern of the as-built alloy (b) DSC curve of the as-built alloy.

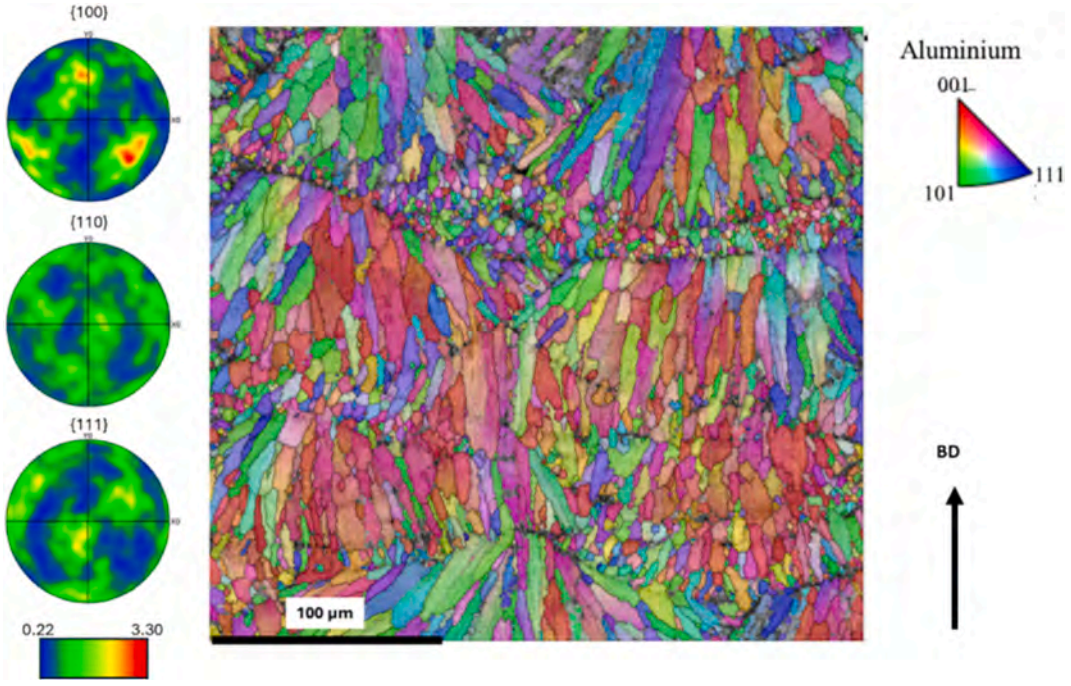

Fig. 7. EBSD map of the as-built alloy and its pole figure, adapted from previous work of the authors [22]

3.3. Heat treatments

Different heat treatments at four different temperatures and various holding times were performed on cubic samples to observe the microstructure transformation when subjected to different heat treatments.

Firstly, a typical T5 treatment was performed. The T5 treatments have been widely reported to improve the aluminium alloy strength [37–39], thanks to the controlled precipitation that hinders dislocation motion without any significant grain growth or loss of silicon network nor supersaturated solution. To achieve this result, the treatment is typically conducted at a temperature not exceeding the first precipitation onset temperature, ensuring that the precipitation potential is fully utilised. The closer the temperature is to the onset temperature, the shorter holding time is needed to reach the hardness peak [6]. For this work, the temperature was then set at 190 °C, which is the exact onset temperature of Si precipitation (peak A in Fig. 6.b). The treatment was performed at different times, i.e. 1, 2, 4 and 8 h.

Then, three different temperatures for annealing treatment were picked. Indeed, aluminium alloys produced by PBF-LB are characterised by phenomenal strength but very low ductility and fracture toughness [12,40,41]. In AlSi9Cu3(Fe), this fragile behaviour is also intensified by the presence of brittle Si precipitates, which, though increasing the strength, tend to decrease the elongation properties [42]. In addition, the high Fe content tends to be detrimental for mechanical characteristics such as toughness and ductility, especially when exciding its critic content, which for an Al alloy with 9.3 % of Si such us the AlSi9Cu3(Fe) used in this study should be 0.65 % [9,42]. To achieve a balance between strength and elongation, heat treatments at higher temperatures, such as annealing, can be performed. Indeed, annealing is typically performed between the upper limit temperature of T5 and the lower temperature for solution heat treatment [43]. Heat treatments between 200 and 400 °C have been reported to homogenise PBF Al-Si parts successfully; in addition, treatment at a temperature lower than 270 °C has been reported to maintain the eutectic Si network, whereas higher

temperatures lead to an improvement in ductility, though at the expense of strength [11,18]. Also, treatments over 415 °C, i.e. a common upper limit of annealing for aluminium alloys, might lead to excessive softening and critical grain growth, making the treatment more similar to a solubilisation [43,44]. Further increasing the temperature to over 450 °C might also lead to porosities increase [12,19,20]. The selected temperatures in this work are then based on the thermal analyses conducted on the as-built samples, and are 250, 300 and 400 °C. Precisely, 250 °C corresponds to the peak temperature for the precipitation of θ'' and Si phases (peak A in Fig. 6.b), while 300 °C marks the onset temperature of θ' precipitation (peak B in Fig. 6.b). Lastly, the choice of treating at 400 °C ensures the complete precipitation of Si, θ'', and θ', while also preventing the formation of undesired phases such as θ-Al_2Cu and potentially Al-Fe, which could compromise the alloy properties. Indeed, when the Al-Cu phase transforms to the thermodynamically stable but incoherent phase θ-Al_2Cu, a drastic decrease in the mechanical properties can be reported due to the reached overageing condition [42,45,46]. These treatment selections, summarised in Table 3, are carefully made to optimise phase formation and preserve the integrity of the alloy, while also being feasible for actual applications.

3.3.1. Direct ageing

T5 is a single-step heat treatment that has been widely employed to improve material hardness. Indeed, the low temperatures retain the fine cellular structure, while simultaneously activating the formation of small precipitates. In addition, this approach preserves the contribution of the supersaturated solid solution to strengthening. However, holding time must be carefully controlled, as prolonged T5 treatments might lead to excessive precipitation, losing supersaturation and causing phases coarsening, detrimental to the final mechanical performance [11,43]. Indeed, once the precipitates begin to coarsen, their contribution to strengthening diminishes as the dislocations adopt the Orowan looping mechanism rather than cutting through the phases [6,47,48].

In this work, the peak hardness has been reached at 190 °C after 1 h, with an increase of about 5 %, from 148.6 HV measured in the as-built material to 155.9 HV after 1 h of treatment, as can be seen in Fig. 8.a. The peak is particularly steep, and the hardness decreased drastically when treated for over two hours, which is attributed to the overageing [6]. Indeed, the unstable microstructure resulting from the oversaturation of the matrix in the as-built material induces an accelerated precipitation mechanism when it is subjected to thermal treatments, strengthening the material by precipitation hardening. In addition, being very close to the temperature where precipitation begins speeds up solute diffusion and phases precipitation. In order to correlate the hardness to the microstructure evolution at different holding times, DSC and SEM image analyses were carried out on heat treated samples.

More detailed assumptions can be made by observing the thermal behaviour after heat treatment through the DSC analysis (Fig. 8.b). It shows that the first peak (peak A in Fig. 6.b) gradually disappeared when the holding time increased, whereas the other peaks remained unaltered even in the sample heat treated for 8 h. This indicates that Si and θ'' compounds tended to precipitate massively already after being heat treated for 1 h since the analysis showed a halved first peak, with a significantly reduced enthalpy, from 7.60 in the as-built to 2.68 J/g. Si and θ'' precipitation was fulfilled after 8 h of heat treatment, as can be observed by the complete disappearance of the peak.

Image analysis allows to identify the microstructure evolution during T5 treatments (Fig. 9). At lower magnification, no differences between as-built and heat treated microstructures could be identified: even after longer heat treatments, MP shapes were still clearly recognisable, with the thinner cellular structure in the centre and coarser in the borders (Fig. 9.a,d,g). However, at higher magnifications, some differences can be highlighted. Already after 1 h of treatment, a higher density of nanoscale Si particles could be spotted in the cells at the MP boundaries, as highlighted in some spots in Fig. 9.c with yellow arrows, confirming the ongoing Si precipitation that had been recorded in the DSC analysis. Indeed, it has already been reported that large amounts of Si and Cu atoms remain trapped in the Al lattice due to the high-speed cooling rates during the PBF-LB process. This entrapment leads to a highly supersaturated matrix, with Si and Cu atoms that tend to diffuse and nucleate into phases even during low-temperature heat treatments, like T5 [49,50]. Also, these small precipitates are the result not only of the precipitation of new Si particles out of the supersaturated Al matrix, but also of the coarsening of already existing nano-sized particles [48]. In addition, the eutectic Si network was entirely unaffected by the heat treatment. On the other hand, after 4 h, some discontinuities in the eutectic Si network began to be evident, becoming even more identifiable after 8 h of heat treatment (Fig. 9.f,i). As a matter of fact, after 8 h, the precipitation of the Si was fully completed, as could be inferred from the disappearance of the first peak in the DSC curve, and the agglomeration of bigger Si particles became significant, as a consequence of the broken Si network. Indeed, the internal energy of the system tends toward a more energetically stable state, which means having a smaller surface energy. To reach this state, the system favours the coalescence of bigger particles, which have low energy thanks to a lower surface-to-volume ratio, instead of structures with high surface energy, such as the Si network [51]. The coalescence and growth of the Si precipitates, in addition to the impoverishment of the supersaturated solid solution, led to the aforementioned hardness drop, inducing overageing. Indeed, after 4 h, the hardness decreased, reverting to a value close to the as-built condition, i.e. 148.8 HV. After 8 h, the weakening of the microstructure became more pronounced, inducing a decrease of 3.5 % compared to the as-built condition, with a hardness of 143.5 HV.

To summarise the observations made, the T5 process significantly improved hardness up to a peak after 1 h of treatment, but prolonged heat exposure led to overageing and a subsequent decline in hardness. The microstructure evolved with the precipitation of Si particles, initially strengthening the material, but as the heat treatment time increased, the coarsening of the precipitates, breaking of the network and depletion of the supersaturated solid solution reduced their strengthening contribution. This behaviour is reflected in both hardness measurements, phase evolution and microstructural changes observed through DSC and SEM, highlighting the critical role of holding time in achieving optimal material properties.

Table 3
Heat treatments design.

As-built (no heat treatment) Temperature (°C)	Holding time (hrs)
190	1–2-4–8
250, 300, 400	0.5–1–2–4

3.3.2. Annealing

As mentioned before, T5 treatments are well known to strengthen the material, thanks to the induced precipitation, without losing the supersaturation of the solution and the characteristic cellular structure. However, no improvement in ductility is usually detected, and in some cases, even a decrease was found, for instance, because of the unwanted precipitation of brittle phases that fasten up the crack propagation when the material is subjected to tensile stress [6], limiting the application of T5 treated material. On the other hand, a treatment that improves material ductility and fracture toughness is annealing. This treatment produces one of the most ductile conditions for aluminium alloys thanks to higher treatment temperatures, usually between the highest ageing temperature and the lowest solubilisation one [43].

In this work, three different temperatures and four different holding times were tested. The effect of the different heat treatments on the hardness is depicted in Fig. 10. As expected, a drastic hardness drop was measured after all heat treatments, which was directly related to the softening caused by the high temperatures, showing their effect even after very short holding times. Indeed, a decrease of hardness could be

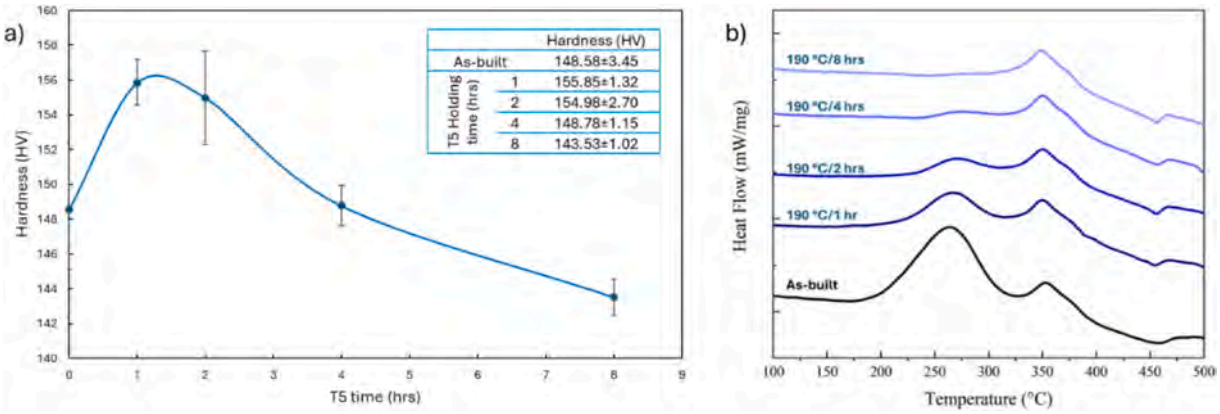

Fig. 8. (a) Hardness curve at different ageing times; (b) DSC of T5 heat treated samples compared with that of the as-built sample.

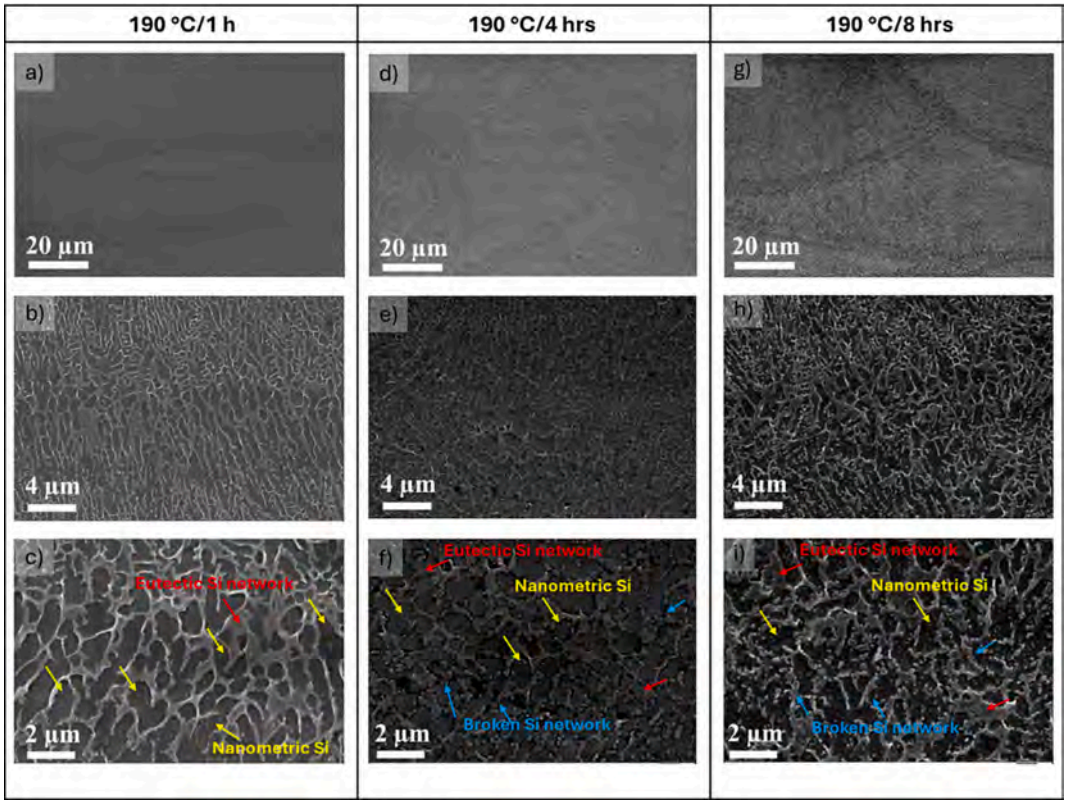

Fig. 9. SEM images at different magnifications of the samples heat treated at 190 °C for 1 h (a-c), 4 h (d-f), 8 h (g-i). Some peculiarity are addressed by the different arrows, like nanometric Si particles (yellow arrows), eutectic Si network (red arrows), broken Si network (blue arrows). (For interpretation of the references to colour in this figure legend, the reader is referred to the web version of this article.)

measured already after 30 min of heat treatment, with a drop of 9.3 % (134.8 HV), 12.7 % (129.8 HV) and 32.3 % (100.6 HV) with treatments at 250, 300 and 400 °C respectively. The values kept decreasing when holding the heat treatment for longer times: when treated for 4 h, a further decrease of the hardness was measured, with an additional reduction of 5 and 7 % for samples treated at 250 and 400 °C respectively, and even an additional 10 % for samples treated at 300 °C, with respect to the corresponding shorter treatments. It can also be observed that the standard deviation tended to be much lower after heat treatments at 400 °C, which was related to a presumable homogenisation of the microstructure that can be guaranteed by the higher temperature, which is closer to typical solubilisation temperatures, like 450 °C [11]. It is also worth noting that the reduction in hardness after treating for 1 h compared to after 30 min is almost negligible for all temperatures. However, a soaking period of at least 1 h is typically employed in heat treatment processes to ensure a more homogenous temperature distribution throughout the sample [43]. Therefore, the ensuing analyses will focus on samples treated with a minimum soaking time of 1 h and a maximum of 4 h.

Thermal analysis by using DSC allowed to analyse the precipitation sequences that had already occurred during the heat treatment. As can be seen in Fig. 11, the first peak, associated to Si and θ''-Al_2Cu precipitation, was entirely absent in all samples, suggesting that both phases have already fully precipitated during the heat treatment. After heat treatments at 250 °C for 1 and 4 h, the second peak was still observed, suggesting that both θ' precipitation and Si spheroidization have not occurred yet during the heat treatment. In contrast, after heat treatment at 300 °C for 1 h, only the peak associated with Si spheroidization could

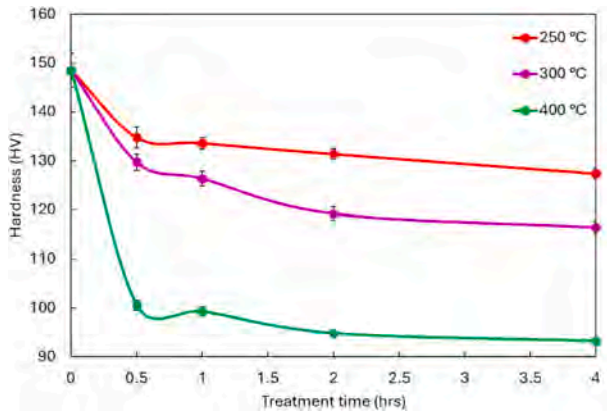

As-built		148.58±3.45 HV		
		Temperature (°C)		
		250	300	400
Holding time (hrs)	0.5	134.78±2.20 HV	129.75±1.68 HV	100.63±1.05 HV
	1	133.63±1.24 HV	126.38±1.48 HV	99.30±0.92 HV
	2	131.40±1.07 HV	119.28±1.35 HV	94.85±0.66 HV
	4	127.40±1.03 HV	116.53±1.17 HV	93.23±0.63 HV

Fig. 10. Hardness curves at different annealing temperatures and times.

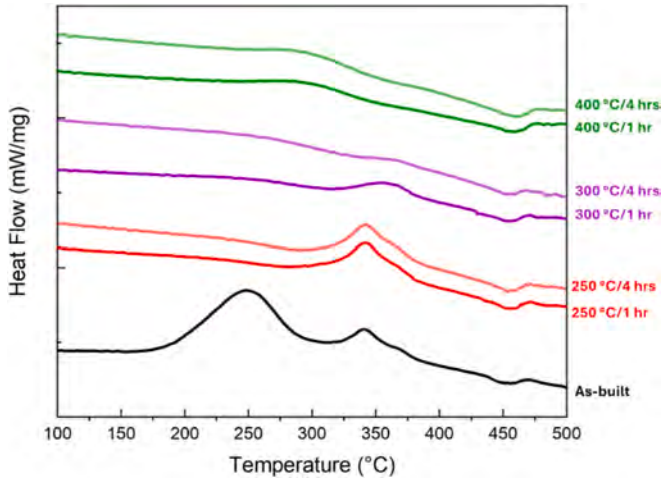

Fig. 11. DSC curves after annealing treatments compared with that of as-built sample.

be identified, indicating a more advanced state of θ precipitation. This peak was completely absent after a longer treatment, leading to the conclusion that the microstructure might be characterised by spheroidised Si particles rather than Si network. At last, treatments at 400 °C led to an almost complete precipitation of phases, with the exception of θ-Al_2Cu, whose peak was still recognisable after each heat treatment.

Image analysis is required to observe and discuss the evolution of the microstructure when subjected to increasing treatment time and temperature (Fig. 12). After 1 h of heat treatment, significant changes in the microstructure can already be observed for samples treated at all temperatures. At lower magnifications, MP shapes were still recognisable after each heat treatment. It was also evident how the microstructure maintained the cellular network in heat treated materials at 250 and 300 °C, with coarser cells at the melt pool boundaries and smaller ones in the centre. On the other hand, the network completely disappeared in samples treated at 400 °C; nonetheless, the typical fish-scale shape was still visible. Indeed, phases tended to precipitate and grow first at the MP boundaries, following their shapes. In contrast, the ones in the MP centre precipitated and coalesced more heterogeneously. At 250 °C, fine precipitates within the cells were visible, similar to those noted during the T5 treatment (Fig. 12.a,b). The network remained mostly continuous, although signs of breakage were beginning to appear in several locations, especially along thinner lines. Indeed, treatments below 270 °C have been reported not to drastically affect the eutectic Si network [5]. On the other hand, in the sample treated at 300 °C, the network was almost entirely discontinuous, and Si precipitates from the network spheroidised (Fig. 12.e,f). The higher temperature likely facilitated the complete precipitation of Si, shifting the internal energy equilibrium towards network breakdown. This resulted in a complete disintegration of the network and activated the spheroidization of the particles. This process aligns with the previous observations of the disappearance of the first peak and the presence of a second, lower-energy peak noted during the DSC analysis. At 400 °C, the cellular structure was completely dismantled; however, as aforementioned, the MP shape was still recognisable thanks to the preferential precipitation of phases at MP borders (Fig. 12.i,l). Indeed, big darker phases could be seen at the MP borders, big up to 1 μm; in the MP centre, dispersed precipitates of different sizes and shapes can be spotted. The higher temperatures allowed a complete precipitation, as could be inferred from the disappearance of the precipitation peaks during the DSC analysis: the already precipitated phases tend to coalesce and grow in size, leading to bigger precipitates.

A few changes can be observed after the heat treatment at 250 °C for longer treatment times. The network was partially broken but still clearly present, and Si nanoprecipitates kept nucleating inside the cells (Fig. 12.c,d). This observation is in accordance with the work of Fiocchi et al. [18], who observed a preserved, though fragmented, eutectic Si network for heat treatment at 250 °C with much higher holding time, i.e. 8 and 64 h. On the other hand, a few differences can also be observed at 400 °C for longer holding times: indeed, fewer and bigger precipitates can be identified, which have grown upon longer treatment through the Ostwald ripening mechanism [11] (Fig. 12.m,n). However, the influence of longer treatment time on the microstructure becomes more evident for heat treatment at 300 °C. The MP shape is still clearly observable at lower magnification (Fig. 12.g), but the differences become undoubtedly evident when observing at higher magnification (Fig. 12.h). The fragmentation of the network was completed, and Si precipitates spheroidization and coalescence through Ostwald ripening mechanism was ongoing. Indeed, instead of the continuous network and the nanometric precipitates, bigger and more spheric particles were observed, which confirms what was already suggested by the DSC, where the peak associated with the Si spheroidization was not present. It can also be highlighted that the samples heat treated at 300 °C were also the ones displaying the highest hardness drop when treated for 4 h compared to after 30 min, i.e. minus about 10 %, which could be explained with the highest microstructural differences in samples treated at different times, compared to the other two treatment temperatures.

Afterwards, XRD analysis was also conducted to identify the phases in each heat treated sample (Fig. 13). It can be observed that longer treatment and higher temperature led to the appearance of new, small peaks. In addition, a higher intensity of the peaks already observed in the as-built alloy, i.e. fcc-Al, diamond cubic Si and tetragonal θ-Al_2Cu, was recorded, though the latter kept having an intensity lower than 3 %. The higher intensity of the peaks indicates a higher presence of the

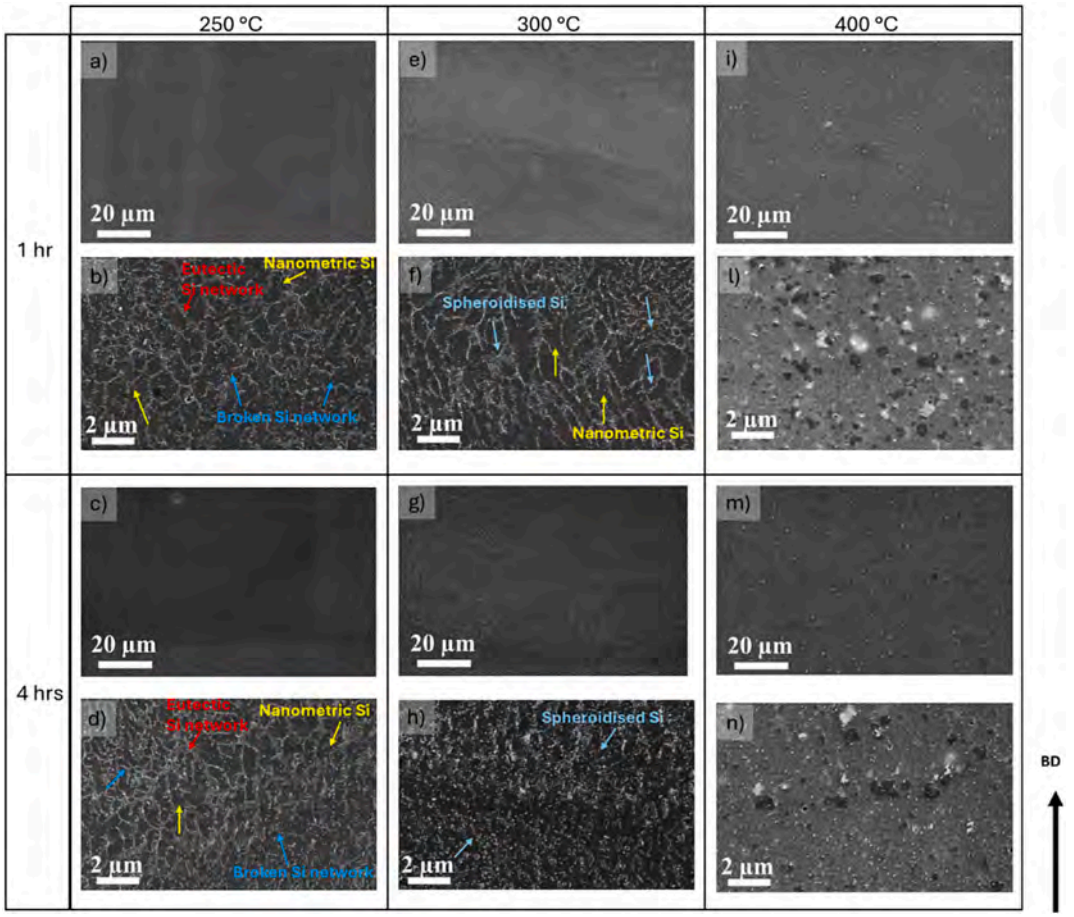

Fig. 12. SEM images at different magnifications of annealed samples, following heat treatment at 250 °C for 1 h (a,b) and 4 h (c,d), at 300 °C for 1 h (e,f) and 4 h (g, h), at 400 °C for 1 h (i,l) and 4 h (m,n). Some peculiarity are addressed by the different arrows, like nanometric Si particles (yellow arrows), eutectic Si network (red arrows), broken Si network (blue arrows), spheroidised Si (light blue arrows). (For interpretation of the references to colour in this figure legend, the reader is referred to the web version of this article.)

phases, which became more detectable. In particular, Si peaks became narrower and more intense, due to the high precipitation rate affected by the heat treatment. This became even more evident for heat treatment at 400 °C, thanks to a high Si particle coalescence that generated a more intense signal during the analysis. It is interesting to dwell on the Si (220) peak, located at about 47° (Fig. 13.b). As aforementioned, the intensity of the peak in the as-built material suggested that the peak, being broader because of the lower signal, overlapped with the Al_2Cu (310) peak. However, it can be noted that at a low treatment time and temperature, the Si peak became narrower, allowing the Cu peak to be recognisable. The more the Si peak became intense, the more the Al_2Cu one was visible, as can be undoubtedly observed in the sample treated at 400 °C for 4 h, where the two peaks were completely independent. It can also be observed that the Al peaks tended to gradually shift towards lower angles when samples were subjected to higher treatment temperatures, as can be seen for peak Al (200) (Fig. 13.c). This shift is a consequence of the diffusion of Cu and Si atoms out of the supersaturated solution, which induced a release on the Al lattice, since both Cu and Si, but also Fe, have a smaller atomic radium than Al [52–54]. Indeed, the measured lattice parameter clearly increases after each heat treatment (Fig. 13.d) compared to the as-built state, suggesting the lattice relaxation due to the full precipitation of Si and θ''-Al_2Cu that occurred after these heat treatments, as evidenced by the complete disappearance of the first peak in the DSC curves (Fig. 11). However, lower lattice parameters when increasing the treatment temperatures can also be observed. The effect of Si precipitation on the parameter is the same after all heat treatments, since Si has fully precipitated after all of them, as demonstrated by the disappearance of the associated peak in the DSC (Fig. 11). On the other hand, only a minor amount of Cu and Fe are still in solid solution after heat treatment at higher temperatures, mostly to fulfil the precipitation sequence of the θ phase, while the remaining has already precipitated. However, the more pronounced precipitation of Cu and Fe during these heat treatments might not result in any significant lattice release compared to treatments at lower temperatures. On the other hand, it can be inferred that other elements in solid solution, such as Mg, might precipitate during these heat treatments, since Mg precipitation has the effect of decreasing the Al lattice parameter, instead of increasing it. Nonetheless, it is not possible to unequivocally confirm the presence of Mg-phases based solely on this observation, since no other significant evidence has been reported.

Low-intensity peaks associated with minor phases tended to appear when treating at higher temperatures. However, their intensity did not exceed 2 %, thus suggesting that, even though they precipitated in higher percentages for longer and higher temperatures treatments, these phases kept being in small amounts and reduced size, making their detection through XRD less efficient. They are presumably associated with minor Al-Cu-Fe phases, in particular N-Al_7Cu_2Fe, $Al_{23}CuFe_4$ and Al_8Fe_5 [55], though their characteristic acicular shape could not be unequivocally spotted in the image analysis. Other minor phases detected in literature for similar alloys could be associated with some of these minor peaks, like $Al_{15}(FeMn)_3Si_2$ [56], Al_8Fe_2Si [57], and β-Mg_2Si and Q- $Al_4Cu_2Mg_8Si_7$ [55], though the small amount of Mg and Mn and higher Cu content in the present alloy makes their presence less likely. It must be highlighted that the reduced amount of these minor phases and

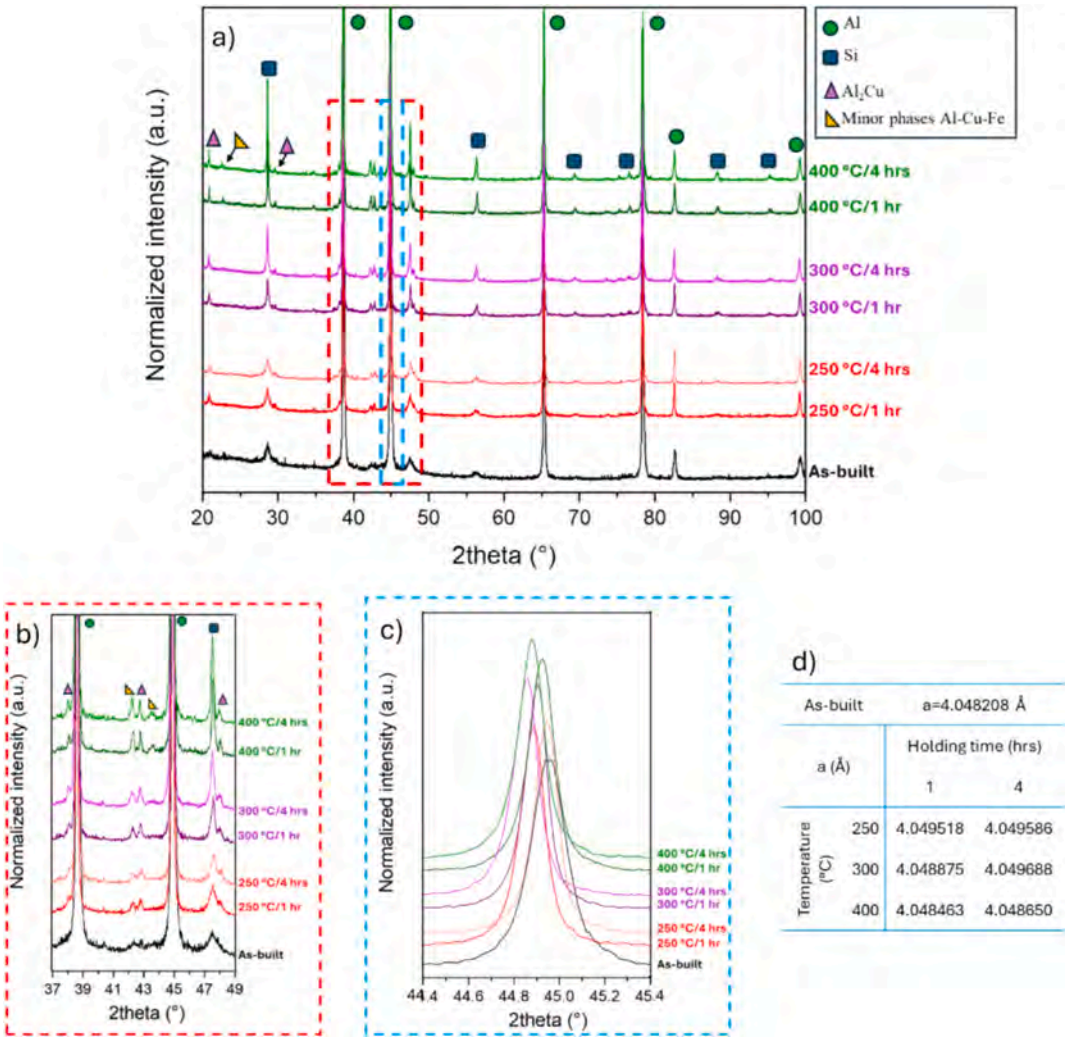

Fig. 13. (a) XRD pattern of annealed samples (b) detail of peaks between 37 and 49° (c) detail of peak Al (220), showing the peak shift after annealing, (d) table of measured Al lattice parameter, in particular, the as-built one and after heat treatments for 1 and 4 h.

the consequent low signal did not allow for confirmation of their presence through only XRD analysis; more advanced detection techniques, like TEM, should be introduced in future works to confirm or dismiss their presence entirely. Nonetheless, previous studies on similar alloys have tried to detect minor phases through this sophisticated analysis [12,15]. They managed to identify Si and Al_2Cu phases clearly and to detect Fe content on as-built, but failed to identify the actual composition of these phases rich in Fe [15]. However, they managed to precisely identify these phases after a T6 treatment, thanks to the massive growth of the precipitates. In particular, they detected the phases Al_5FeSi, Al_7Cu_2Fe and Al_8Fe_5 [12]. So, it can be presumed that these phases might also be present in the present work, though in a radically smaller size and amount due to lower temperatures applied.

In summary of the findings, annealing processes result in significant changes in the material microstructure, reducing the hardness. Materials heat treated at 400 °C showed the lowest hardness results, caused by the complete disappearance of the Si network and the depletion of the supersaturated solution, and an improved homogenisation of the microstructure, with larger phases more homogenously dispersed in the material. This heat treatment also led to a higher degree of precipitation of Si and other phases rich in Cu and Fe. At 300 °C, the treatment time has more evident effects, with an almost complete disintegration of the network at a shorter time and a full dismantling and advanced spheroidization of the Si particles for longer times. At 250 °C, the treatment led to the partial breakage of the cellular network, with fine precipitates forming within the cells.

3.4. Selected heat treatments

To further investigate the impact of heat treatment on the material, more detailed analyses were performed on samples treated at four different temperatures for a selected holding time. Specifically, EBSD was used to observe grain modifications, while tensile tests assessed how heat treatments influenced the material static mechanical behaviour.

For the T5 heat treatment, a holding time of 1 h was chosen, as it corresponds to the peak hardening time. The same treatment time was picked for the annealing processes, in order to achieve adequate softening without significantly compromising the material strength, while also improving the feasibility of the industrial process.

3.4.1. EBSD after selected heat treatments

Fig. 14 shows the EBSD maps of Al grain structure along the building direction after 1-hour heat treatment and their polar figure plot, each with the indication of the MUD parameter for the intensity of weaving. It can be observed that the two distinct grain areas, i.e. small equiaxed grains at the MP borders and elongated larger grains inside the MPs, remained clearly distinguishable even after all heat treatments. Additionally, a small amount of grain growth was measured after each heat treatment for both Equivalent Circle Diameter (ECD) and Feret diameter, as shown in Table 4. However, it is important to highlight that the

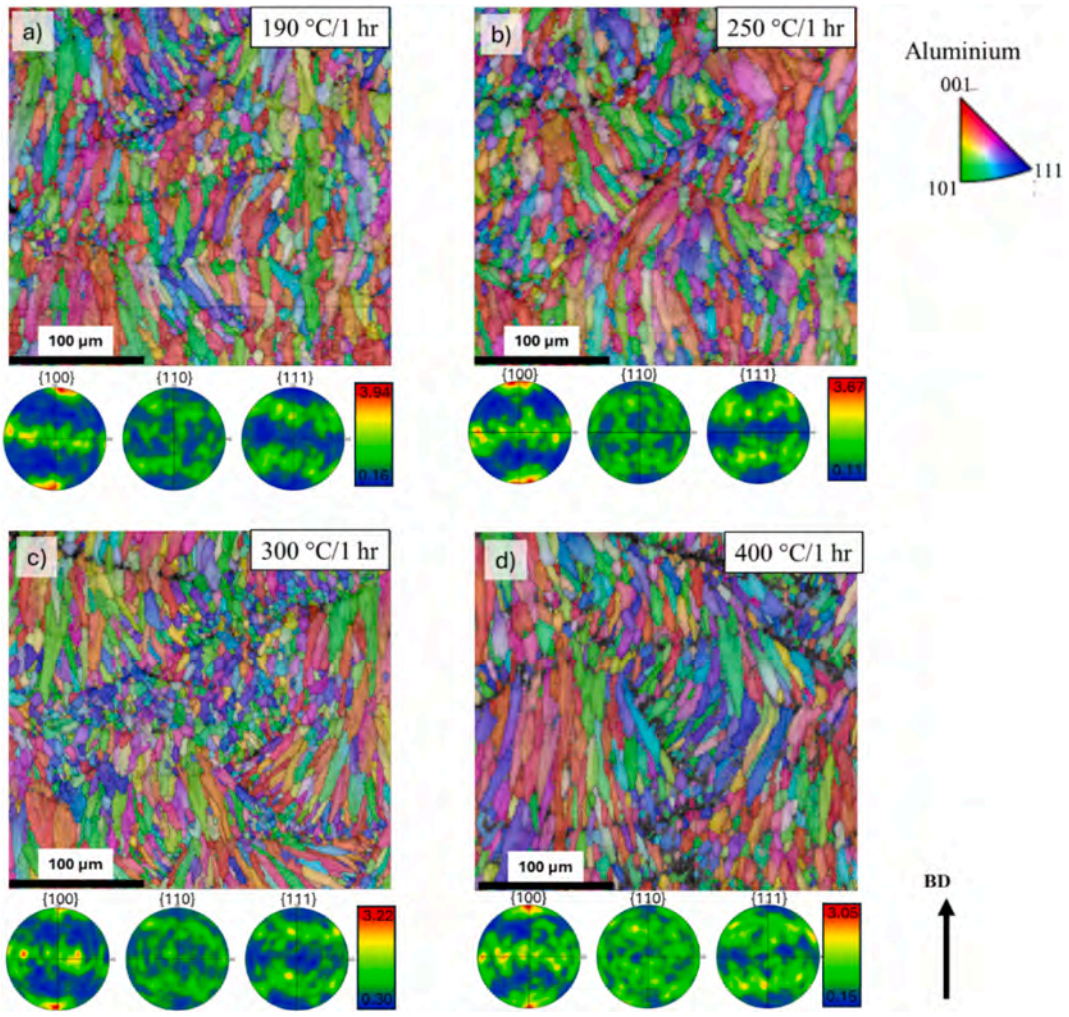

Fig. 14. EBSD maps and relative pole figures of heat treated samples:(a)190 °C/1 hr, (b)250 °C/1 hr, (c)300 °C/1 hr, (d)400 °C/1 hr.

Table 4
Grain size after heat treatments.

	Avarage Feret Diameter (µm)	Avarage ECD (µm)	Max Feret Diameter (µm)	Max ECD (µm)
As-built	12.12 ± 10.95	7.29 ± 4.68	136.35	35.57
190 °C/1 hr	17.86 ± 13.08	9.66 ± 5.34	114.73	41.13
250 °C/1 hr	14.82 ± 10.96	8.50 ± 4.84	79.16	33.83
300 °C/1 hr	15.45 ± 11.95	8.96 ± 4.95	111.32	36.85
400 °C/1 hr	15.85 ± 14.66	8.37 ± 5.26	168.61	38.42

reported variations in grain size were minimal and fell within the range of the standard deviation. Therefore, the differences in results can be more likely attributed to the variability in local grain size. These observations support the assumption that the heat treatment does not affect grain growth, as has already been observed during the heat treatment of other aluminium alloys [18,58,59]. Indeed, as reported by Takata et al. [60], the eutectic Si particle acts as an inhibitor for the Al grain growth, limiting their growth even at higher treatment temperatures. Nonetheless, after the heat treatment at 400 °C, some larger grains were observed, reaching even a maximum Feret diameter of 169 µm. This might be attributed to the complete disappearance of the Si network, which resulted in the precipitation of larger and more dispersed particles, thereby reducing the inhibitory effect on grain growth.

Observing the pole figure, a preferential orientation along the {001} direction can be identified for the elongated grains along the building direction, as per other Al alloys [18,58,61,62]. It can also be observed that the MUD parameter, which is dependent on the intensity of the grain weaving, tended to decrease slightly for higher temperature treatment, going from 3.94 after heat treatment at 190 °C to 3.05 after 400 °C-treatment. This can be correlated to a homogenisation of the microstructure at higher temperatures and minor recrystallisation, with the nucleation and growth of grains with different orientations, which led to a weakening of the weaving [63].

3.4.2. *Tensile tests after selected heat treatments*

The static mechanical behaviour was evaluated through tensile tests, with the results reported in Table 5 and Fig. 15. As aforementioned, the BS EN 1706:2020 + A1:2021 standard states minimum requirements for the mechanical behaviour of an AlSi9Cu3(Fe), i.e. a YS of 140 MPa, a UTS of 240 MPa and a minimum ε of 1.00 %. The as-built sample not only utterly satisfied the standard requirements but also outperformed the yield and tensile strength of most AlSi9Cu3(Fe) alloys produced by casting [13,64,65], having a YS of 298 MPa, a UTS of 429 MPa and an elongation to failure of 2.97 %. However, as expected, the elongation was still very low, in some cases even lower than the cast counterpart [64], a symptom of the poor toughness of the as-built alloy and a possibly negative influence during the tests of the samples internal

Table 5
Measured mechanical properties of as-built and annealed samples, with reported variations of the annealed ones compared to the as-built (YS tensile yield strength, UTS ultimate tensile strength, ε elongation to fracture, Kf modulus of toughness).

	YS (MPa) Mean	Std Dev	UTS (MPa) Mean	Std Dev	ε (%) Mean	Std Dev	K_f (MJ/m^3)
As-built	298.2	4.3	429.5	1.6	2.97	0.13	10.79
190 °C/1 hr	303.0 (+2 %)	1.7	408.3 (−5 %)	8.8	2.27 (−24 %)	0.16	8.07 (−25 %)
250 °C/1 hr	250.2 (−16 %)	4.4	384.8 (−10 %)	5.4	2.90 (−2 %)	0.27	9.20 (−14 %)
300 °C/1 hr	231.9 (−22 %)	2.9	384.4 (−11 %)	5.2	4.65 (+57 %)	0.14	14.34 (+33 %)
400 °C/1 hr	156.3 (−48 %)	1.1	308.7 (−28 %)	2.9	11.58 (+290 %)	0.93	26.93 (+150 %)

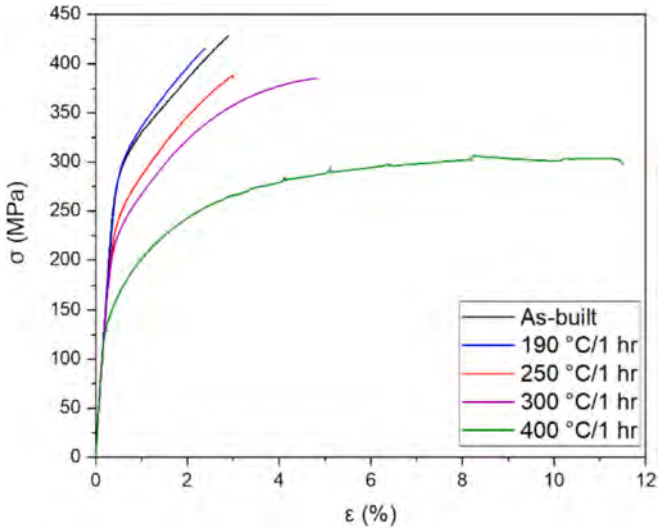

Fig. 15. Tensile curve of as-built and heat treated.

defects, that even if limited have still an impact on the final performance. The outstanding results, especially compared to as cast alloy, have already been reported in literature for other Al alloys [66,67], and are the result of the peculiar microstructure resulting from the process. Indeed, the extremely fine cellular structure acts as strengthening for the alloy, significantly improving the mechanical performance. Furthermore, the continuous and dense network hinders the dislocation movement, generating a dense area of dislocation that strengthens the material [11]. In addition, the supersaturated solid solution has been reported to increase the strength of aluminium alloys further [64].

Various trends can be reported compared to similar AlSi9Cu3(Fe) produced per PBF-LB in previous works. Indeed, the present study showed a better performance compared to the as-built AlSi9Cu3(Fe) produced by Roudnicka et al. [12], with a reported YS of 219 MPa, UTS of 374 MPa and an e of 2.50 %, but a worse one compared to Fiocchi et al. [16], who reported a higher UTS of 462 MPa and a e of 4.50 %, but a lower YS of 266 MPa. These differences might be explained by the different setups of the tests compared to the present work or by the different quality of the final samples in terms of densification and surface quality. It can also be observed that Fiocchi et al. worked with an AlSi9Cu3 alloy with a low amount of Fe, i.e. 0.339 %; this might result in a better mechanical behaviour of the alloy compared to the one used in the present work, which is characterised by a higher Fe content, i.e. 0.91 %. In fact, a high iron content has been reported to negatively impact the tensile strength and the ductility of the alloy, although leaving the yield strength unaffected [9].

The various heat treatments affected the mechanical behaviour in different ways. The T5 treatment at 190 °C implied a decrease in the material performance, with a worse UTS, i.e. 408.3 MPa, and especially a lower fracture elongation, i.e. 2.27 %, though also showing a slightly higher YS, i.e. 303 MPa. Indeed, the still intact cellular network and the coherent θ'' phases kept strengthening the alloy, the former due to dislocation pile-up along the network boundaries, the latter because of precipitation strengthening. At the same time, the decrease in ductility suggests that the new brittle Si precipitates detected inside the cells (Fig. 9.c), though strengthening the alloy by precipitation hardening, tended to make it more fragile, decreasing the elongation at fracture [6,11,12].

When treated at 250 °C, samples are characterised by a lower strength, i.e. YS of 250.2 MPa and UTS of 384.8 MPa. The alloy heat treated for 1 h at 250 °C was characterised by a higher concentration of nanoscale Si particles inside the cells and a partial network breakage (Fig. 12.b). The discontinuities in the network, which reduced the dislocation concentration at the boundaries and thus its effectiveness in strengthening the alloy, caused the reported decrease in the alloy strengths. In addition, the higher amount of Si and Cu-rich phases, inferred by the XRD and DSC analyses (Fig. 11,13), suggests a lower solute concentration in the solid solution, therefore causing a reduction of the solid solution strengthening mechanism. However, an elongation close to the one measured for the as-built alloy was reported. Indeed, the fine and fragile Si particles still affect the alloy plasticity, keeping the elongation to a low 2.90 % [12,61].

Similarly, a strength decrease was measured for samples treated at 300 °C, i.e. YS 231.9 MPa and UTS 384.4 MPa. Compared to the heat treatment at 250 °C, only the YS showed a decrease, whereas UTS reported similar values. The heat treatment at 300 °C was reported to imply the formation of a higher amount of Si and Cu-rich precipitates, as demonstrated by the higher XRD peaks (Fig. 13) and the disappearance of the first two exothermic peaks in the DSC curve (Fig. 11), and a completely discontinuous Si network mainly consisting of globular precipitates (Fig. 12.f). The impoverishment of the solid solution [61] and the disappearance of the continuous network [53,68] are directly related to the strength decrease. In addition, DSC analyses presumed a higher amount of θ' phases over θ″ phases, unlike what was observed in the alloy heat treated at 250 °C: this might further decrease the alloy yield strength compared to the 250 °C-treated material, since a higher percentage of θ″ phases have been reported to be correlated to a higher alloy strength, whereas semi-coherent θ' has a less effective strengthening mechanism [17]. However, an improvement in ductility was also measured, with an almost doubled elongation at fracture compared to the as-built sample, i.e. 4.65 %. Indeed, the gradual Si spheroidization has been reported to increase the ductile failure over the fragile one [13]. The larger space between particles and the softening of the matrix better accommodates the dislocations mobility, thus improving the material ductility.

A further improvement in ductility, i.e. 11.58 %, at the expense of strength, i.e. YS 156.3 MPa and UTS 308.7 MPa, was reported for the alloy treated at 400 °C for 1 h. The alloy microstructure was characterised by a complete disappearance of the network and a massive coalescence of precipitates, with Si and Cu-rich phases as big as a couple of microns and distant from each other, significantly improving the ductility by facilitating the dislocation movement [69] (Fig. 12.l). It can also be observed by the stress–strain curve (Fig. 15) that serrated plastic flow on stress tends to appear in the plastic deformation. These fluctuations have already been reported for other alloys and identified as

Portevin-Le Chatelier effect. Reported by Le Chatelier in the early 1900 s, this effect describes a fluctuation of the mechanical behaviour of alloys under stress caused by interaction between dislocations and atoms in solid solution or fine coherent precipitates [70,71]. It can be presumed that fine Al_2Cu phases and the other nanometric phases detected by XRD were responsible for the effect. Finally, it must be noticed that even if the strength was heavily affected by the heat treatment, it still satisfied the standard requirements.

At last, the simplified modulus of toughness K_f, defined as strain energy per area before fracture, was evaluated and reported in Table 5 by using the formula of Oh [72], where instead of integrating the area under the tensile curve, the area is estimated as the sum of smaller rectangular areas:

$$K_f = \varepsilon(\sigma_y + \sigma_{UTS})/2$$

As expected, a decrease in toughness was measured after T5, where higher strength and lower elongation had been recorded. This confirms that the material was strengthened by the heat treatment, though experiencing a relevant embrittlement that caused the decrease in toughness. The annealing at 250 °C is also reported to cause a decrease in toughness compared to the as-built condition, caused by the softening of the material, with a decrease in its strength and no variation in its elongation at fracture. On the other hand, the annealing treatments at 300 and 400 °C improved toughness, with an increase of 33 and even 150 %, respectively. Indeed, the material exhibits a softening, with lower strengths, due to the network dismantle and the matrix impoverishment. However, at the same time, an improvement in elongation was registered thanks to facilitating dislocations movement, increasing the area below the curve, meaning that major energy was absorbed before fracture. This increase is particularly evident after the heat treatment at 400 °C, with the highest recorded elongation and modulus of toughness.

In conclusion, all heat treatments satisfied the minimum requirements of the BS EN 1706:2020 + A1:2021 standard for AlSi9Cu3 (Fe) alloys. However, it was demonstrated that heat treatments tailored the AlSi9Cu3(Fe) alloy mechanical response, offering trade-offs between strength and ductility (Fig. 16), making the alloy suitable for different applications in the automotive field [73–76]. The as-built condition outperformed the heat treated samples in terms of strength due to the fine cellular structure and supersaturated solid solution, though showing poor ductility. The impressive strength makes it ideal for parts that require good resistance without high toughness, such as engine blocks, mostly produced with materials that show an elongation of only 1.2–2.3 % in light of an YS and a UTS of at least 180–300 and 230–345 MPa, respectively [77,78], or gearboxes [79]. On the other hand, the highest elongation was reached after the heat treatment at 400 °C for 1 h, a heat treatment that caused a major improvement in toughness but also a significant weakening. This heat treatment is advisable for applications that require a higher toughness and that are not subjected to major stresses, such as engine cradle, that are generally produced with material characterised by an elongation of at least 6–10 %, a YS of 120 MPa and a UTS of 250 MPa [74–80]. Finally, the heat treatment at 300 °C ensures a good compromise between strength and ductility, with a not too significant strength loss compared to the as-built condition and, on the other hand, an improved toughness, though the elongation keeps being not too high. The resulting mechanical properties allow the material to support high static loads, maintaining a minimal ductility, which can be ideal for applications such as steering boxes, that usually require an elongation of at least 1.5–3 %, a YS of 150–210 MPa and a UTS of 240–300 MPa [81,82].

4. Conclusion

The study investigated the influence of different heat treatments on the microstructure and mechanical properties of the PBF-LB processed AlSi9Cu3(Fe) alloy. Key findings are summarised as follows:

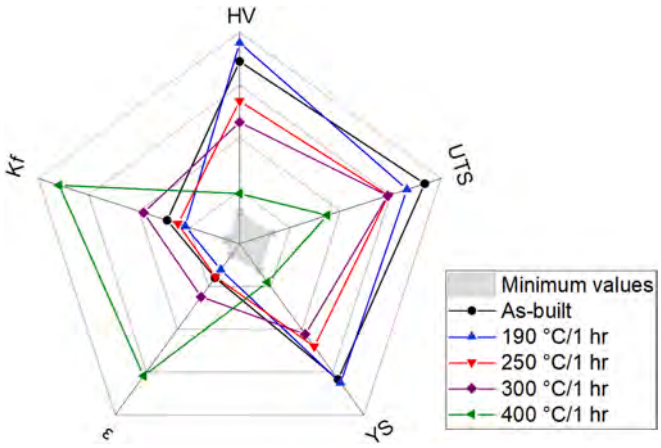

Fig. 16. Radar diagram of the main properties of the AlSi9Cu3(Fe) alloy in the as-built state and after heat treatments, compared to the minimum ones defined by BS EN 1706:2020 + A1:2021 standard: HV (80–160 HV), UTS (200–450 MPa), YS (100–350 MPa), ε (0–15 %), Kf (0–30 MJ/m^3).

- The as-built microstructure exhibited a fine cellular network of α-Al surrounded by eutectic Si, with distinct MP boundaries. The rapid cooling rates inherent to the PBF-LB process resulted in a supersaturated solid solution and fine grain sizes, contributing to the alloy exceptional strength (UTS 429 MPa) but limited ductility (2.97 %).
- Direct ageing enhanced the material hardness due to the precipitation of Si and θ'' phases. Peak hardness (155.9 HV) was achieved after 1 h of treatment, attributed to the dense precipitation and retention of the fine cellular structure. Prolonged holding times led to overageing, characterised by phase coarsening, network disruption, and hardness decline. Microstructural analyses revealed that fine Si particles contributed to strengthening during short treatments, though negatively affecting ductility.
- Annealing at higher temperatures enhanced ductility while reducing hardness and strength. Treatments at 250 °C partially preserved the eutectic Si network, resulting in minimal strength reduction (UTS 384.8 MPa). After the heat treatment at 300 °C, the Si network underwent extensive fragmentation, forming spheroidised particles that greatly improved elongation to fracture (4.65 %), though slightly decreasing the strength (UTS 384.4 MPa). This temperature achieved the best balance between maintaining adequate strength and enhancing plasticity. Finally, treatment at 400 °C led to the complete disappearance of the cellular network, the coalescence of precipitates, and significant softening, leading to drastic strength reduction (UTS 308.7 MPa). However, ductility impressively increased to 11.58 %, driven by the improved dislocation mobility in the homogenised matrix.

Declaration of competing interest

The authors declare the following financial interests/personal relationships which may be considered as potential competing interests: Diego Giovanni Manfredi reports financial support was provided by European Union. If there are other authors, they declare that they have no known competing financial interests or personal relationships that could have appeared to influence the work reported in this paper.

Acknowledgments

This work was funded by the European Union – NextGenerationEU, under the National Recovery and Resilience Plan (NRRP), Mission 4, Component 2, Investment 1.1, funding call PRIN 2022 D.D. 104

published on 2.2.2022 by the Italian Ministry of University and Research (Ministero dell'Università e della Ricerca), Project Title: Tailor-made Light Alloys for Light Vehicles Modular Design – CUP E53D23005300001

Appendix

.

Table A1
Porosity results of the full DOE.

Sample	Laser Power (W)	Scan Speed (mm/s)	Hatch Distance (mm)	Porosity (%)	Std Dev (%)
A1	170	800	0.10	1.23	0.06
A2	190	800	0.10	0.66	0.08
A3	170	800	0.12	0.40	0.10
A4	190	800	0.12	0.23	0.04
A5	170	800	0.14	0.68	0.07
A6	190	800	0.14	0.23	0.10
B1	170	1000	0.10	1.04	0.02
B2	190	1000	0.10	0.60	0.01
B3	170	1000	0.12	0.96	0.03
B4	190	1000	0.12	0.27	0.08
B5	170	1000	0.14	1.13	0.10
B6	190	1000	0.14	0.17	0.07
C1	170	1200	0.10	1.52	0.10
C2	190	1200	0.10	0.60	0.10
C3	170	1200	0.12	2.28	0.04
C4	190	1200	0.12	0.23	0.05
C5	170	1200	0.14	3.05	0.05
C6	190	1200	0.14	0.60	0.06
D1	170	1400	0.10	2.25	0.04
D2	190	1400	0.10	0.54	0.07
D3	170	1400	0.12	3.65	0.08
D4	190	1400	0.12	0.53	0.06
D5	170	1400	0.14	5.45	0.02
D6	190	1400	0.14	2.18	0.02

Data availability

Data will be made available on request.

References

[1] H.R. Kotadia, G. Gibbons, A. Das, E.P.D. Howes, A review of Laser Powder Bed Fusion Additive Manufacturing of aluminium alloys: Microstructure and properties, Addit. Manuf. 46 (2021) 102155, https://doi.org/10.1016/j.addma.2021.102155.

[2] R.S. Rana, Rajesh Purohit, and S Das, Reviews on the Influences of Alloying elements on the Microstructure and Mechanical Properties of Aluminum Alloys and Aluminum Alloy Composites, Int. J. Sci. Res. Publ. 2 (6) (2012) 1–7.

[3] O. S. I. Fayomi, A. P. I. Popoola, e N. E. Udoye, «Effect of Alloying Element on the Integrity and Functionality of Aluminium-Based Alloy», in *Aluminium Alloys - Recent Trends in Processing, Characterization, Mechanical Behavior and Applications*, S. Sivasankaran, A c. di, InTech, 2017. doi: 10.5772/intechopen.71399.

[4] S. Hegde, E.K.N. Prabhu, Modification of eutectic silicon in Al–Si alloys, J. Mater. Sci. vol. 43, fasc. 9 (2008) 3009–3027, https://doi.org/10.1007/s10853-008-2505-5.

[5] K.G. Prashanth, et al., Microstructure and mechanical properties of Al–12Si produced by selective laser melting: effect of heat treatment, Mater. Sci. Eng. A 590 (2014) 153–160, https://doi.org/10.1016/j.msea.2013.10.023.

[6] F. Bosio, P. Fino, D. Manfredi, E.M. Lombardi, Strengthening strategies for an Al alloy processed by in-situ alloying during laser powder bed fusion, Mater. Des. 212 (2021) 110247, https://doi.org/10.1016/j.matdes.2021.110247.

[7] A. Martucci, E. Bassini, E.M. Lombardi, Effect of Cu Content on the PBF-LB/M Processing of the Promising Al-Si-Cu-Mg Composition, Metals vol. 13, fasc. 7 (2023) 1315, https://doi.org/10.3390/met13071315.

[8] B. Callegari, T.N. Lima, E.R.S. Coelho, «The Influence of Alloying elements on the Microstructure and Properties of Al-Si-based Casting Alloys, A Review», Metals vol. 13, fasc. 7 (2023) 1174, https://doi.org/10.3390/met13071174.

[9] J. A. Taylor, «The Effect of Iron in Al-Si Casting Alloys».

[10] P. Wei, et al., The AlSi10Mg samples produced by selective laser melting: single track, densification, microstructure and mechanical behavior, Appl. Surf. Sci. 408 (2017) 38–50, https://doi.org/10.1016/j.apsusc.2017.02.215.

[11] J. Fiocchi, A. Tuissi, e C. A. Biffi,, Heat treatment of aluminium alloys produced by laser powder bed fusion: a review, Mater. Des. 204 (2021) 109651, https://doi.org/10.1016/j.matdes.2021.109651.

[12] M. Roudnická, O. Molnárová, D. Dvorský, L. Křivský, e D. Vojtěch,, Specific Response of Additively Manufactured AlSi9Cu3Fe Alloy to Precipitation Strengthening, Met. Mater. Int. vol. 26, fasc. 8 (2020) 1168–1181, https://doi.org/10.1007/s12540-019-00504-y.

[13] M. Panušková, E. Tillová, e M. Chalupová,, Relation between mechanical properties and microstructure of cast aluminum alloy AlSi9Cu3, Strength Mater. vol. 40, fasc. 1 (2008) 98–101, https://doi.org/10.1007/s11223-008-0026-8.

[14] J. Suchy, L. Pantelejev, D. Palousek, D. Koutny, e J. Kaiser,, Processing of AlSi9Cu3 alloy by selective laser melting, Powder Metall. vol. 63, fasc. 3 (2020) 197–211, https://doi.org/10.1080/00325899.2020.1792675.

[15] M. Fousova, D. Dvorsky, M. Vronka, D. Vojtech, e P. Lejcek,, The use of Selective Laser Melting to increase the Performance of AlSi9Cu3Fe Alloy, Materials vol. 11, fasc. 10 (2018) 1918, https://doi.org/10.3390/ma11101918.

[16] J. Fiocchi, C.A. Biffi, e A. Tuissi,, Selective laser melting of high-strength primary AlSi9Cu3 alloy: Processability, microstructure, and mechanical properties, Mater. Des. 191 (2020) 108581, https://doi.org/10.1016/j.matdes.2020.108581.

[17] M. Roudnicka, D. Dvorsky, e D. Vojtech,, The effect of heat treatment on the microstructure and mechanical properties of 3D-printed AlSi9Cu3Fe alloy, IOP Conf. Ser.: Mater. Sci. Eng. 461 (2018) 012071, https://doi.org/10.1088/1757-899X/461/1/012071.

[18] J. Fiocchi, et al., Heat Treatments for stress Relieving AlSi9Cu3 Alloy Produced by Laser Powder Bed Fusion, Materials vol. 14, fasc. 15 (2021) 4184, https://doi.org/10.3390/ma14154184.

[19] F. Bosio, C. Phutela, N. Ghisi, A. Alhammadi, e N. T. Aboulkhair,, Tuning the microstructure and mechanical properties of AlSi10Mg alloy via in-situ heat-treatments in laser powder bed fusion, Mater. Sci. Eng. A 879 (2023) 145268, https://doi.org/10.1016/j.msea.2023.145268.

[20] G. Di Egidio, L. Ceschini, A. Morri, C. Martini, e M. Merlin,, A Novel T6 Rapid Heat Treatment for AlSi10Mg Alloy Produced by Laser-based Powder Bed Fusion: Comparison with T5 and conventional T6 Heat Treatments, Metall. Mater. Trans. B vol. 53, fasc. 1 (2022) 284–303, https://doi.org/10.1007/s11663-021-02365-6.

[21] *R. Leardi, C. Melzi, G. Polotti, CAT (Chemometric Agile Tool), freely downloadable from http://gruppochemiometria.it/index.php/software*.

[22] I. Lagalante, E. Ghinatti, A. Martucci, R. Bertolini, S. Bruschi, e M. Lombardi, «On the Role of Additive Manufacturing, Heat Treatment and Machining on the

Microstructural Evolution and Corrosion Behaviour of AlSi9Cu3(Fe) alloy», *Material Characterization*, vol. 224, 2025, doi: https://doi.org/10.1016/j.matchar.2025.115089.
[23] D.J. Burgess, E. Duffy, F. Etzler, e A. J. Hickey,, Particle size analysis: AAPS workshop report, cosponsored by the Food and Drug Administration and the United States Pharmacopeia, AAPS J. vol. 6, fasc. 3 (2004) 23–34, https://doi.org/10.1208/aapsj060320.
[24] Z. Xiang, M. Zhang, R. Yan, Q. Yin, e K. Zhang,, Powder-spreading dynamics and packing quality improvement for laser powder bed fusion additive manufacturing, Powder Technol. 389 (2021) 278–291, https://doi.org/10.1016/j.powtec.2021.05.036.
[25] K. Riener, et al., Influence of particle size distribution and morphology on the properties of the powder feedstock as well as of AlSi10Mg parts produced by laser powder bed fusion (LPBF), Addit. Manuf. 34 (2020) 101286, https://doi.org/10.1016/j.addma.2020.101286.
[26] F. Chu, et al., Influence of satellite and agglomeration of powder on the processability of AlSi10Mg powder in Laser Powder Bed Fusion, J. Mater. Res. Technol. 11 (2021) 2059–2073, https://doi.org/10.1016/j.jmrt.2021.02.015.
[27] S. Vaudreuil, S.-E. Bencaid, H.R. Vanaei, e A. El Magri,, Effects of Power and Laser speed on the Mechanical Properties of AlSi7Mg0.6 Manufactured by Laser Powder Bed Fusion, Materials vol. 15, fasc. 23 (2022) 8640, https://doi.org/10.3390/ma15238640.
[28] E. Li, Z. Zhou, L. Wang, R. Zou, e A. Yu,, Modelling of keyhole dynamics and melt pool flow in laser powder bed fusion process, Powder Technol. 400 (2022) 117262, https://doi.org/10.1016/j.powtec.2022.117262.
[29] N.T. Aboulkhair, N.M. Everitt, I. Ashcroft, e C. Tuck,, Reducing porosity in AlSi10Mg parts processed by selective laser melting, Addit. Manuf. 1–4 (2014) 77–86, https://doi.org/10.1016/j.addma.2014.08.001.
[30] D. Schimbäck, et al., An improved process scan strategy to obtain high-performance fatigue properties for Scalmalloy®, Mater. Des. 224 (2022) 111410 https://doi.org/10.1016/j.matdes.2022.111410.
[31] A. Mertens, J. Delahaye, O. Dedry, B. Vertruyen, J.T. Tchuindjang, e A. M. Habraken,, Microstructure and Properties of SLM AlSi10Mg: Understanding the Influence of the local thermal history, Procedia Manuf. 47 (2020) 1089–1095, https://doi.org/10.1016/j.promfg.2020.04.121.
[32] J. Delahaye, J.T. Tchuindjang, J. Lecomte-Beckers, O. Rigo, A.M. Habraken, e A. Mertens,, Influence of Si precipitates on fracture mechanisms of AlSi10Mg parts processed by Selective Laser Melting, Acta Mater. 175 (2019) 160–170, https://doi.org/10.1016/j.actamat.2019.06.013.
[33] L. Thijs, K. Kempen, J.-P. Kruth, e J. Van Humbeeck,, Fine-structured aluminium products with controllable texture by selective laser melting of pre-alloyed AlSi10Mg powder, Acta Mater. vol. 61, fasc. 5 (2013) 1809–1819, https://doi.org/10.1016/j.actamat.2012.11.052.
[34] M. Tang e P. C. Pistorius,, Anisotropic Mechanical Behavior of AlSi10Mg Parts Produced by Selective Laser Melting, JOM vol. 69, fasc. 3 (2017) 516–522, https://doi.org/10.1007/s11837-016-2230-5.
[35] N. J. Luiggi A.,, A Preliminary Study of the phase Transformations in rolled Al-Fe-Si Alloy, Metall. Mater. Trans. A vol. 41, fasc. 13 (2010) 3271–3275, https://doi.org/10.1007/s11661-010-0496-8.
[36] J. Wang, et al., A crack-free and high-strength Al-Cu-Mg-Mn-Zr alloy fabricated by laser powder bed fusion, Mater. Sci. Eng. A 854 (2022) 143731, https://doi.org/10.1016/j.msea.2022.143731.
[37] H. Zhang, et al., Achieving superior mechanical properties of selective laser melted AlSi10Mg via direct aging treatment, Journal of Materials Science & Technology 108 (2022) 226–235, https://doi.org/10.1016/j.jmst.2021.07.059.
[38] H. Tang, et al., Effects of direct aging treatment on microstructure, mechanical properties and residual stress of selective laser melted AlSi10Mg alloy, Journal of Materials Science & Technology 139 (2023) 198–209, https://doi.org/10.1016/j.jmst.2022.08.032.
[39] T.-H. Park, M.-S. Baek, H. Hyer, Y. Sohn, e K.-A. Lee,, Effect of direct aging on the microstructure and tensile properties of AlSi10Mg alloy manufactured by selective laser melting process, Mater Charact 176 (2021) 111113, https://doi.org/10.1016/j.matchar.2021.111113.
[40] J. Suryawanshi, K.G. Prashanth, S. Scudino, J. Eckert, O. Prakash, e U. Ramamurty,, Simultaneous enhancements of strength and toughness in an Al-12Si alloy synthesized using selective laser melting, Acta Mater. 115 (2016) 285–294, https://doi.org/10.1016/j.actamat.2016.06.009.
[41] H. Chen, S. Patel, M. Vlasea, e Y. Zou,, Enhanced tensile ductility of an additively manufactured AlSi10Mg alloy by reducing the density of melt pool boundaries, Scr. Mater. 221 (2022) 114954, https://doi.org/10.1016/j.scriptamat.2022.114954.
[42] S. Gain, T.E.F. Silva, A.M.P. Jesus, A. Cavaleiro, P.A.R. Rosa, e A. Reis,, Mechanical characterization of the AlSi9Cu3 cast alloy under distinct stress states and thermal conditions, Eng. Fract. Mech. 216 (2019) 106499, https://doi.org/10.1016/j.engfracmech.2019.106499.
[43] «Heat Treating of Aluminum Alloys, ASM Handbook, Volume 4: Heat Treating ASM Handbook Committee, p 841-879 DOI: 10.1361/asmhba0001205».
[44] W. Li, et al., Effect of heat treatment on AlSi10Mg alloy fabricated by selective laser melting: Microstructure evolution, mechanical properties and fracture mechanism, Mater. Sci. Eng. A 663 (2016) 116–125, https://doi.org/10.1016/j.msea.2016.03.088.
[45] D. Shin, A. Shyam, S. Lee, Y. Yamamoto, e J. A. Haynes,, Solute segregation at the Al/θ′-Al2Cu interface in Al-Cu alloys, Acta Mater. 141 (2017) 327–340, https://doi.org/10.1016/j.actamat.2017.09.020.
[46] L. Jiang, Z. Zhao, e G. Wang,, The Effects on Stability and Electronic Structure of Si-Segregated θ′/Al Interface Systems in Al-Cu Alloys, Coatings vol. 14, fasc. 7 (2024) 879, https://doi.org/10.3390/coatings14070879.
[47] A. Abd El-Aty, Y. Xu, X. Guo, S.-H. Zhang, Y. Ma, e D. Chen,, Strengthening mechanisms, deformation behavior, and anisotropic mechanical properties of Al-Li alloys: a review, J. Adv. Res. 10 (2018) 49–67, https://doi.org/10.1016/j.jare.2017.12.004.
[48] G. Di Egidio, L. Tonelli, M. Zanni, D. Carosi, A. Morri, e L. Ceschini,, Direct artificial aging of the PBF-LB AlSi10Mg alloy designed to enhance the trade-off between strength and residual stress relief, Journal of Alloys and Metallurgical Systems 5 (2024) 100063, https://doi.org/10.1016/j.jalmes.2024.100063.
[49] S. Marola, et al., Alloying AlSi10Mg and Cu powders in laser Single Scan Tracks, melt spinning, and Laser Powder Bed Fusion, J. Alloy. Compd. 821 (2020) 153538, https://doi.org/10.1016/j.jallcom.2019.153538.
[50] R. Casati e M. Vedani,, Aging Response of an A357 Al Alloy Processed by Selective Laser Melting, Adv. Eng. Mater. vol. 21, fasc. 4 (2019) 1800406, https://doi.org/10.1002/adem.201800406.
[51] D. Lehmhus, T. Rahn, A. Struss, P. Gromzig, T. Wischeropp, e H. Becker,, High-Temperature Mechanical Properties of Stress-Relieved AlSi10Mg Produced via Laser Powder Bed Fusion Additive Manufacturing, Materials vol. 15, fasc. 20 (2022) 7386, https://doi.org/10.3390/ma15207386.
[52] A.M. Samuel, H.W. Doty, S. Valtierra, e F. H. Samuel,, Defects related to incipient melting in Al–Si–Cu–Mg alloys, Mater. Des. 1980–2015 (52) (2013) 947–956, https://doi.org/10.1016/j.matdes.2013.05.048.
[53] P. Ma, et al., Influence of Annealing on Mechanical Properties of Al-20Si Processed by Selective Laser Melting, Metals vol. 4, fasc. 1 (2014) 28–36, https://doi.org/10.3390/met4010028.
[54] X. Yang, Y. Cheng, X. He, K. Yang, e R. Zong,, Effect of Heat Treatment on the Microstructure, Compressive Property, and Energy Absorption Response of the Al–Mg–Si Alloy Foams, Adv. Eng. Mater. vol. 23, fasc. 2 (2021) 2000620, https://doi.org/10.1002/adem.202000620.
[55] F. Bosio, I. Lagalante, D. Manfredi, e M. Lombardi,, Bespoke multi-step homogenization heat-treatment for a laser powder bed fused AlSi10Mg4Cu alloy synthesized via in-situ alloying, Mater Charact 195 (2023) 112506, https://doi.org/10.1016/j.matchar.2022.112506.
[56] E. Tillov, M. Chalupov, e L. Hurtalov, «Evolution of Phases in a Recycled Al-Si Cast Alloy During Solution Treatment», in *Scanning Electron Microscopy*, V. Kazmiruk, A c. di, InTech, 2012. doi: 10.5772/34542.
[57] L.H. Pereira, et al., Influence of Fe content on the microstructure and mechanical properties of Al-7Si-0.7Mg-2.8Fe alloy processed by laser powder bed fusion, Mater. Sci. Eng. A 893 (2024) 146152, https://doi.org/10.1016/j.msea.2024.146152.
[58] N. Takata, M. Liu, H. Kodaira, A. Suzuki, e M. Kobashi,, Anomalous strengthening by supersaturated solid solutions of selectively laser melted Al–Si-based alloys, Addit. Manuf. 33 (2020) 101152, https://doi.org/10.1016/j.addma.2020.101152.
[59] K.V. Yang, P. Rometsch, C.H.J. Davies, A. Huang, e X. Wu,, Effect of heat treatment on the microstructure and anisotropy in mechanical properties of A357 alloy produced by selective laser melting, Mater. Des. 154 (2018) 275–290, https://doi.org/10.1016/j.matdes.2018.05.026.
[60] N. Takata, H. Kodaira, K. Sekizawa, A. Suzuki, e M. Kobashi,, Change in microstructure of selectively laser melted AlSi10Mg alloy with heat treatments, Mater. Sci. Eng. A 704 (2017) 218–228, https://doi.org/10.1016/j.msea.2017.08.029.
[61] M. Liu, T. Wada, A. Suzuki, N. Takata, M. Kobashi, e M. Kato,, Effect of Annealing on Anisotropic Tensile Properties of Al–12%Si Alloy Fabricated by Laser Powder Bed Fusion, Crystals vol. 10, fasc. 11 (2020) 1007, https://doi.org/10.3390/cryst10111007.
[62] M.J. Paul, et al., Fracture resistance of AlSi10Mg fabricated by laser powder bed fusion, Acta Mater. 211 (2021) 116869, https://doi.org/10.1016/j.actamat.2021.116869.
[63] M. Zhang, et al., Grain refinement and mechanical properties improvement of AlCuFeCoNi high-entropy alloy coatings fabricated by resonant ultrasonic assisted laser cladding, Opt. Laser Technol. 182 (2025) 112233, https://doi.org/10.1016/j.optlastec.2024.112233.
[64] M. Zamani, S. Seifeddine, e A. E. W. Jarfors,, High temperature tensile deformation behavior and failure mechanisms of an Al–Si–Cu–Mg cast alloy — the microstructural scale effect, Mater. Des. 86 (2015) 361–370, https://doi.org/10.1016/j.matdes.2015.07.084.
[65] M. Voncina, A. Nagode, e M. Bizjak, «Dependence of mechanical properties on Cu content in AlSi9Cu3(Fe) alloy», *Teh. vjesn.*, vol. 24, fasc. Supplement 1, 2017, doi: 10.17559/TV-20140922143741.
[66] C.C. Roth, T. Tancogne-Dejean, e D. Mohr,, Plasticity and fracture of cast and SLM AlSi10Mg: High-throughput testing and modeling, Addit. Manuf. 43 (2021) 101998, https://doi.org/10.1016/j.addma.2021.101998.
[67] H. Barhoumi, S. Souissi, M.B. Amar, e F. Elhalouani,, Influence of heat treatment on the microstructures and mechanical properties of squeeze cast AlSi9Cu3 alloys, IJMMP vol. 10, fasc. 5/6 (2015) 472, https://doi.org/10.1504/IJMMP.2015.074999.
[68] V.J. Matjeke, C. Moopanar, A.S. Bolokang, e J. W., Van Der Merwe, «effect of heat treatment time on the microstructure and mechanical deformation behavior of additive-manufactured AlSi10Mg components», Prog. Addit. Manuf. vol. 5, fasc. 4 (2020) 379–385, https://doi.org/10.1007/s40964-020-00139-1.
[69] X.G. Cui, et al., Microstructure and tensile properties of the sub-micro and nano-structured Al produced by laser surface melting, Mater. Sci. Eng. A vol. 527, fasc. 27–28 (2010) 7400–7406, https://doi.org/10.1016/j.msea.2010.08.008.
[70] P. Zhang, G. Liu, e J. Sun,, A critical review on the Portevin-Le Chatelier effect in aluminum alloys, J. Cent. South Univ. vol. 29, fasc. 3 (2022) 744–766, https://doi.org/10.1007/s11771-022-4977-x.

[71] Z. Hu, Y. Qi, X. Nie, H. Zhang, e H. Zhu,, The Portevin-Le Chatelier (PLC) effect in an Al-Cu aluminum alloy fabricated by selective laser melting, Mater Charact 178 (2021) 111198, https://doi.org/10.1016/j.matchar.2021.111198.
[72] G. Oh, A simplified toughness estimation method based on standard tensile data, Int. J. Press. Vessel. Pip. 199 (2022) 104733, https://doi.org/10.1016/j.ijpvp.2022.104733.
[73] A.A. Luo, Recent advances in light metals and manufacturing for automotive applications, CIM Journal vol. 12, fasc. 3 (2021) 79–87, https://doi.org/10.1080/19236026.2021.1947088.
[74] F. Casarotto, A.J. Franke, e R. Franke,, «High-pressure die-cast (HPDC) aluminium alloys for automotive applications», in *Advanced Materials in Automotive Engineering*, Elsevier (2012) 109–149, https://doi.org/10.1533/9780857095466.109.
[75] W. Zhang e J. Xu,, Advanced lightweight materials for automobiles: a review, Mater. Des. 221 (2022) 110994, https://doi.org/10.1016/j.matdes.2022.110994.
[76] J. Hajkowski P. Popielarski e R. Sika, Prediction of HPDC Casting Properties made of AlSi9Cu3 Alloy . in Advances in Manufacturing, A. Hamrol, O. Ciszak, S. Legutko, e M. Jurczyk, A c. Di Lecture Notes in Mechanical Engineering 2018 Springer International Publishing Cham 621 631 10.1007/978-3-319-68619-6_59.
[77] S. Kianfar, E. Aghaie, J. Stroh, D. Sediako, e J. Tjong,, Residual stress, microstructure, and mechanical properties analysis of HPDC aluminum engine block with cast-in iron liners, Mater. Today Commun. 26 (2021) 101814, https://doi.org/10.1016/j.mtcomm.2020.101814.
[78] R. González, et al., Fatigue of an aluminium cast alloy used in the manufacture of automotive engine blocks, Int. J. Fatigue 54 (2013) 118–126, https://doi.org/10.1016/j.ijfatigue.2013.03.018.
[79] R. Masoudi Nejad, K. Aliakbari, S.K. Abbasnia, e J. Langari,, Failure analysis of overdrive gear of passenger car gearbox fabricated from powder metallurgy, Eng. Fail. Anal. 141 (2022) 106683, https://doi.org/10.1016/j.engfailanal.2022.106683.
[80] A. Zovi e F. Casarotto, «SILAFONT-36, THE LOW IRON DUCTILE DIE CASTING ALLOY DEVELOPMENT AND APPLICATIONS».
[81] F. Sanna, A. Fabrizi, S. Ferraro, G. timelli, e P. Ferro, F. Bonollo,, «Multiscale characterisation of AlSi9Cu3(Fe) die casting alloys after Cu, Mg, Zn and Sr addition», vol. La, Metall. Ital. 105 (4) (2013) 13–24.
[82] I. Vicario I. Anza F. Sáenz de Tejada e J. C. García, H. Galarraga, M. Merchán, Development of New Al-Si9Cu3 Alloys for HPDC Components with Tailored Properties 2014 Bilbao, Spain.